Hindawi
Journal of Engineering
Volume 2023, Article ID 8238703, 28 pages
https://doi.org/10.1155/2023/8238703

Research Article

Stagnation Point Flow of $CoFe_2O_4/TiO_2$-H_2O-Casson Nanofluid past a Slippery Stretching/Shrinking Cylindrical Surface in a Darcy–Forchheimer Porous Medium

Kifle Adula Duguma[1] **Oluwole Daniel Makinde**[2] **and Lemi Guta Enyadene**[1]

[1]*Department of Applied Mathematics, Adama Science and Technology University, Adama, Oromia, Ethiopia*
[2]*Faculty of Military Science, Stellenbosch University, Stellenbosch, South Africa*

Correspondence should be addressed to Kifle Adula Duguma; kifle.adula@astu.edu.et

Received 3 July 2023; Revised 5 September 2023; Accepted 21 September 2023; Published 6 October 2023

Academic Editor: Abdullah A. Kendoush

Mounting temperatures in electronic devices during operation may damage sensitive internal components if too much thermal energy accumulates inside the system. The advent of an innovative ultrahigh-performance thermal management technology known as nanofluid has provided a veritable platform to improve the system performance and reliability by removing the high heat flux generated in the engineering and industrial devices. This paper examines the combined effects of Darcy–Forchheimer porous medium-resistant heating and viscous dissipation on stagnation point flow of a Casson nanofluid ($CoFe_2O_4$-H_2O and TiO_2-H_2O) towards a convectively heated slippery stretching/shrinking cylindrical surface in a porous medium. The governing nonlinear model equations are obtained, analysed, and tackled numerically via the shooting technique with the Runge–Kutta–Fehlberg integration scheme. A unique solution is obtained when the surface is stretching. For shrinking cylindrical surface, the model exhibits nonunique dual solutions for a defined range of parameter values, and a temporal stability analysis is conducted to ascertain the stable and physically achievable solution. The effects of emerging thermophysical parameters on the overall flow structure and thermal management such as velocity and temperature profiles, skin friction, and Nusselt number are quantitatively discussed through graphs and in tabular form. It is found that the thermal performance heat transfer enhancement capability of TiO_2-H_2O is higher than that of $CoFe_2O_4$-H_2O. Moreover, the nanofluid thermal performance is enhanced with nanoparticles volume fraction, Casson nanofluid parameter, and Biot number but lessened with porous medium permeability.

1. Introduction

Non-Newtonian fluids have various applications: damping and braking devices, printing technology, personal protective equipment, food products, and drag-reducing agents. Casson fluids are used to characterize non-Newtonian fluids with shear-thinning properties. Nakamura and Sawada [1] studied non-Newtonian fluid and introduced the biviscosity model as a constitutive equation (1) for blood instead of the usually used Casson model equation for blood. Animasaun [2] studied incompressible Casson fluid flow with viscous dissipation and obtained that the temperature profile reduces as the Casson parameter rises. Rasool et al. [3] discussed the heat and mass transfer characteristics of Casson-type MHD nanofluid flow. Recently, Khan et al. [4] and Alkasasbeh [5] also studied Casson-type fluid flow.

Due to the advancement of thermal devices in engineering systems, the applications of nanofluids have been playing a vital role in the enhancement of heat transfer and cooling processes of electronic devices in many manufacturing industry processes (Tadesse et al.) [6]. Nanoparticles provide a huge surface area for heat transfer because of their special features, such as lower density and excellent chemical and physical stabilities. For instance, due to its hard magnetic material with high coercivity and good mechanical stabilities at higher temperature and great chemical and physical stability, cobalt ferrite $CoFe_2O_4$ is the most suitable for several applications: audio, videotape, generator, etc. (Kazemi et al.) [7] and its high thermal conductivity made TiO_2 nanoparticles for use as enhancements in the heat transfer rate and has great applications in the areas of paints and coatings, cooling of radiators and electronic devices, nucleate pool boiling, heat exchangers, preparation of sunscreen, catalysts, etc. (Ali et al.) [8]. Mebarek-Oudina and Chabani [9] reviewed nanofluid applications and heat transfer enhancement techniques in different enclosures, and they concluded that porous media and nanofluid properties have a direct relation with flow enhancement and heat transfer-boosting impacts. Ganesh et al. [10] carried out a boundary layer analysis to investigate the influences of slip and viscous flow on water-based MHD nanofluid, and Jawad et al. [11] investigated variable heat transmission in MHD nanofluid flow. Furthermore, the Darcy–Forchheimer flow of Sisko nanofluid with convective thermal boundary conditions and viscous dissipation was investigated, and it was revealed that Darcy number enhanced while the Forchheimer number reduced the rate of heat transfer, and the values of Darcy number controls the skin friction as discussed by Bisht and Sharma [12]. Singh et al. [13] assessed nonuniform heat source and melting heat transfer on magnetized Cu-H_2O nanofluid and obtained that an increment in porous media parameter values, the heat transfer rate, and surface drag force diminished near the surface of the cylinder. Moreover, it was observed that an augmentation in Reynolds number *Re* declined the surface drag force and raised Nusselt number (heat transfer rate). Poornima et al. [14] mathematically studied heat transfer in boundary-layer stagnation flow past a stretching/shrinking cylinder and found that the coefficients of drag force and the heat transfer rate at the surface enhanced with an augmentation in Reynolds number. Most recently, Najib et al. [15] investigated stagnation point nanofluid flow past an exponentially shrinking/stretching cylinder inserted, and they discovered that as the slip parameter rised, the skin friction coefficient dropped, whereas the heat transfer coefficient enhanced. Moreover, the heat transfer and skin friction coefficients increased with the larger nanoparticle volume fraction and curvature parameter, and the Cu nanoparticle has the highest coefficient of skin friction and heat transfer rate. Our recent articles Duguma et al. [16, 17] detailed about the applications of non-Newtonian Casson nanofluids.

For their various practical applications in the areas of polymer technology, metallurgy, chemical engineering, industrial processes, etc., boundary layer fluid flow due to stretching-shrinking/stretching has received due attention for the last few decades (Tadesse et al.) [6]. According to Jawad et al. [11], the stretching surface is formed by boundary layer flows, which usually occur in various engineering applications such as the sketching of plastic films, pseudofibers, permanent casting, glass blowing, metal spinning, etc. Weidman et al. [18] considered uniform shear flow past a stretching sheet surface, and Das et al. [19] characterized the fluid flow over an inclined, exponentially stretching flat surface. Fluid flow towards a shrinking case is possible due to stagnation point flow (Wang [20]). According to him, even though no possible solution is found for the unconfined fluid flow occurring in the boundary layer of the shrinking surface, due to the addition of stagnation flow, a nonunique solution exists. Lund et al. [21] studied nanofluid flow across an exponentially contracting sheet surface and demonstrated that multiple solutions exist. Moreover, they investigated that as the shrinking rate increases, convective heat transfer drops due to an augmentation in the thickness of the boundary layer. Ganesh et al. [10] carried out a boundary layer analysis to investigate the influences of slip and viscous flow of water-based MHD nanofluid past a stretching/shrinking surface and discovered dual solutions under different conditions of stretching/shrinking and suction/injection parameters. Ferdows et al. [22] studied a biomagnetic fluid (blood taken as a base fluid and $CoFe_2O_4$ as magnetic particles) flow and heat transfer through a stretching/shrinking cylinder. Najib et al. [15] investigated the impact of stretching/shrinking surfaces on the nanofluid flow and demonstrated that as slip and curvature parameters enhance, the range of the upper branch solutions expands.

The study of flow at the stagnation point (which means fluid flow over a solid surface stagnation area) of nanofluids has many applications in plastic sheet extrusion, manufacturing and industrial processing, aerodynamics, cooling and drying of paper products, etc. [6]. Gorla [23] made an analysis for the steady-state heat transfer in an axisymmetric stagnation flow on a circular cylinder. Gorla [24] investigated the boundary layer solutions for the axisymmetric stagnation mixed convection flow past a vertical cylinder. Again, Harris et al. [25] considered the steady mixed convection stagnation point boundary layer flow on an impermeable surface with slip. Moreover, Shatnawi et al. [26] made a mathematical analysis of the stagnation point flow of Casson nanofluid flow over a vertical Riga plate surface and solved it using the bvp4c technique built into Matlab packages. Basha and Sivaraj [27] numerically investigated the dual solutions and stability analysis over the extending/contracting wedge and stagnation point for the Casson nanofluid flow. Murad et al. [28] solved the heat transfer properties of Casson–Carreau fluid at the stagnation point over a continuous moving plate surface. More on stagnation point boundary layer flows, the existence of dual solutions, and stability analysis are discussed in [14, 16, 29–39].

For decades, convective heat transfer through a porous medium has attracted the interest of scientists due to its numerous applications in fields such as nuclear waste repositories, thermal insulation, solar power, geophysics, pollutant dispersion in aquifers, ground hydrology, grain storage devices, high-performance building insulation, chemical catalytic reactors, cooling of electronic systems, fossil fuel beds, petroleum reservoirs, aerodynamic heat shielding, etc. (Hussain and Sheremet [40]). The fluid flow regime through a porous space was first studied by Darcy (Darcy's law, for small Reynolds numbers) and then later developed to consider large Reynolds numbers (Darcy–Forchheimer model), as discussed in Das et al. [19]. Hayat et al. [41] studied the Cattaneo–Christov heat flux model for flow past a porous medium and obtained that as the values of the porosity parameter enhance, the velocity profile and momentum boundary layer thickness are reduced while the temperature profile falls. Mebarek and Chabani [9] reviewed nanofluid applications and heat transfer enhancement techniques in different enclosures, and they concluded that porous media and nanofluid properties have a direct relationship with flow enhancement and heat transfer boosting impacts. Another study [4] investigated theoretically the Casson nanofluids flow past a vertical Riga plate embedded in porous medium and obtained that as permeability of the porous medium (Darcy number) increased, velocity profile increases (and drops for increment in nanoparticle volume fraction), and the drag force reduced for enhancement in porous medium parameters. Another study [42] presented MHD Newtonian fluid flow on a vertical sheet in the porous medium. They observed that as the velocity slip, curvature of the cylinder, and the porosity enhanced the velocity and temperature profiles and their boundary layer, and the drag force dropped, respectively. Lund et al. [21] analysed the impact of Darcy–Forchheimer on the flow of two-dimensional MHD nanofluid across an exponentially shrinking sheet surface and deduced that the velocity profile was reduced for enhancing the permeability parameter of the porous media. More discussion on the effects of porous media on non-Newtonian Casson nanofluids was found in our recent works (Duguma et al.) [16, 17].

In recent years, great interest has been developed in the study of convective fluid flow due to its applications in geophysics, techniques of oil recovery, heat storage systems, engineering of thermal insulation, etc. Moreover, numerous industrial and environmental systems such as geothermal energy systems, heat exchanger design, geophysics, fibrous insulation, catalytic reactors, etc. involve convection flow through porous media. Merkin [43] made an investigation into the existence of dual solutions in mixed convection in a porous medium. Makinde [44] theoretically investigated the stagnation point hydromagnetic flow of Fe_3O_4-water past a convectively heated permeable shrinking/stretching sheet and revealed that dual solutions exist for a certain range of stretching/shrinking parameters ($\lambda_c < \lambda < 0$) and confirmed that the upper branch solution is temporally stable and physically realizable while the lower branch solution is not. Moreover, he confirmed the existence of a critical shrinking parameter value λ_c below which no real solution occurs. Alizadeh et al. [45] investigated the forced convection of heat flow past cylinders impinging in porous media. Hong et al. [46] investigated the nonlinear mixed convection of heat in a stagnation-point flow past a solid cylinder inserted in a porous medium. More work regarding the convective flow in porous media and its impacts is found in [2, 12, 13].

From the aforementioned literature, no scientific work has been done to consider the collective effects of all embedded parameters under consideration on the complex non-Newtonian Casson nanofluid flow with heat transfer characteristics. The main goal of this paper is to investigate the existence of dual solutions, which is expected due to shrinking surfaces, and apply stability analysis to determine the stable and physically reliable solutions that buttress the theoretical relevance of the work for the hydrodynamic Casson nanofluid flow past a stretching/shrinking slippery surface in a Darcy–Forchheimer porous medium with the presence of viscous dissipation and convective heating using $CoFe_2O_4$-H_2O and TiO_2-H_2O as nanoparticles in comparison, filling the gap of the articles of Duguma et al. [16, 17] with considering cylindrical geometry of flow surface, where the novelty is tested nearer to the critical shrinking parameter $|\lambda_c|$. Moreover, this study brings significant input in the field of chemical and mechanical engineering sciences. Particularly, nanofluids are widely employed in different cooling systems in engineering and in industries for effective heat removal from electronics. For the modeled boundary layer PDEs which were transformed into similar ODEs with their corresponding boundary conditions, the numerical results of similar velocity and thermal profiles, skin friction coefficient, and rates of heat transfer and enhancement were discussed both graphically and quantitatively using the shooting technique with bvp solver embedded in Maple software packages.

2. Mathematical Description of the Problem

Consider a laminar, steady, viscous, incompressible two-dimensional stagnation point flow of $CoFe_2O_4$-H_2O and TiO_2-H_2O Casson nanofluid towards a horizontal linearly stretching/shrinking cylindrical surface in a Darcy–Forchheimer porous medium with surface velocity $U_w = 2bz$ and free stream stagnation point velocity $U_\infty = 2cz$. The flow physical model presented in Figure 1, modified from the model used by Alizadeh et al. [45], is a convectively heated horizontal cylinder embedded in porous media. A cylindrical coordinate system is used, where the axial length of the cylinder (z-axis) is considered in the direction of the stretching/shrinking surface and the dimension (r-axis) is the radial change of the cylinder. The free stream temperature of the fluid flow is taken as T_∞, and the convectively heated temperature of the stretching/shrinking surface of the cylinder is $T_f = T_\infty + nz^2$.

Following Nakamura and Sawada [1] and Animasaun [2], the rheological equation of an incompressible and isotropic flow of a Casson fluid is expressed as follows:

$$\tau_{ij} = \begin{cases} 2\left(\mu_B + \dfrac{p_y}{\sqrt{2\pi}}\right)e_{ij}, & if\ \pi > \pi_c, \\ 2\left(\mu_B + \dfrac{p_y}{\sqrt{2\pi_c}}\right)e_{ij}, & if\ \pi < \pi_c, \end{cases} \quad (1)$$

where τ_{ij} is the component of the stress tensor, μ_B is the plastic dynamic viscosity of the non-Newtonian fluid flow, $\beta \equiv \mu_B\sqrt{2\pi_c}/p_y$ is the non-Newtonian Casson parameter, p_y is the yield stress of the Casson fluid, $\pi = e_{ij}e_{ij}$ is the $(i, j)^{th}$ rate of deformation component (product of strain tensor rate with itself), $e_{ij} = 1/2[\partial u_i/\partial x_j + \partial u_j/\partial x_i]$ is the strain

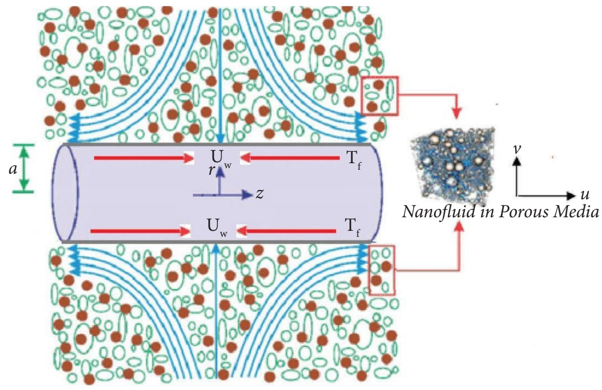

FIGURE 1: Schematic diagram of a stationary cylinder with radial stagnation flow and Casson nanofluid in porous media.

tensor rate, and π_c is a critical value of π, that is defined based on the non-Newtonian model. In the case of Casson fluid flow, $\pi > \pi_c$. The dynamic viscosity is computed as follows: $\mu_f = \mu_B + p_y/\sqrt{2\pi}$. On substitution, the kinematic viscosity becomes $\nu_f = \mu_B/\rho_f(1 + 1/\beta)$. For non-Newtonian Casson fluid flow $\pi > \pi_c$, $\mu = \mu_B + p_y/\sqrt{2\pi}$. Assuming the Darcy–Forchheimer flow model of flows in porous media, for this analysis, the governing equations of this problem are formulated from the balance of continuity, linear momentum, and energy towards a stretching/shrinking cylindrical surface with respect to a cylindrical coordinate $z - r$ system and are given by

$$\frac{\partial ru}{\partial z} + \frac{\partial rv}{\partial r} = 0, \tag{2}$$

$$u\frac{\partial u}{\partial z} + v\frac{\partial u}{\partial r} = U_\infty \frac{dU_\infty}{dz} + \frac{\mu_{nf}}{\rho_{nf}}\left(1 + \frac{1}{\beta}\right)\left(\frac{\partial^2 u}{\partial r^2} + \frac{1}{r}\frac{\partial u}{\partial r}\right) - \frac{\mu_{nf}}{\rho_{nf}k_1}\left(1 + \frac{1}{\beta}\right)(u - U_\infty) - \frac{F}{\rho_{nf}\sqrt{k_1}}(u - U_\infty)^2, \tag{3}$$

$$u\frac{\partial T}{\partial z} + v\frac{\partial T}{\partial r} = \frac{k_{nf}}{(\rho c_p)_{nf}}\left(\frac{\partial^2 T}{\partial r^2} + \frac{1}{r}\frac{\partial T}{\partial r}\right) + \frac{\mu_{nf}}{(\rho c_p)_{nf}}\left(1 + \frac{1}{\beta}\right)\left(\frac{\partial u}{\partial r}\right)^2 + \frac{\mu_{nf}}{(\rho C_p)_{nf}k_1}\left(1 + \frac{1}{\beta}\right)(u - U_\infty)^2 + \frac{F}{(\rho C_p)_{nf}\sqrt{k_1}}(u - U_\infty)^3, \tag{4}$$

subjected to boundary conditions given by

$$\left.\begin{aligned} &u(z,a) = U_w(z) + \frac{\mu_f}{L}\left(1 + \frac{1}{\beta}\right)\frac{\partial u}{\partial r}, v(z,a) = 0 \\ &-k_f\frac{\partial T}{\partial r}(z,a) = h_f\left[T_f(z) - T(z,a)\right] \\ &u(z,\infty) \longrightarrow U_\infty(z), T(z,\infty) \longrightarrow T_\infty \end{aligned}\right\}, \tag{5}$$

where u, v, μ_{nf}, β, ρ_{nf}, k_1, F, k_{nf}, $(\rho C_p)_{nf}$, C_p, μ_f, L, k_f, h_f, a, b, c, and n are the z direction velocity, r direction velocity, effective dynamic viscosity, non-Newtonian/Casson parameter, effective density, permeability of the porous medium, Forchheimer drag force coefficient, effective thermal conductivity, effective heat capacity, specific heat at constant pressure, dynamic viscosity, slip length coefficient, thermal conductivity, convective heat transfer coefficient, radius of the cylinder, constant of strain rate at the cylinder surface, constant of free stream strain rate of the nanoparticles, and real constant (Km^{-2}) of the Casson nanofluid flow, respectively. The parameters k_{nf}, C_p, μ_{nf}, and ρ_{nf} are defined (following Makinde [44], and Tadesse et al. [6]) as follows:

$$k_{nf}=\frac{k_s+2k_f-2\phi\left(k_f-k_s\right)}{k_s+2k_f+\phi\left(k_f-k_s\right)}k_f,\left(\rho C_p\right)_{nf}=(1-\phi)\left(\rho C_p\right)_f+\phi\left(\rho C_p\right)_s \\ \mu_{nf}=\mu_f(1-\phi)^{-2.5},\rho_{nf}=(1-\phi)\rho_f+\phi\rho_s \tag{6}$$

where ρ_f is the density of the base fluid, ρ_s is density of the solid nanoparticle, k_f is the base fluid thermal conductivity, k_s is the nanoparticles thermal conductivity, ϕ is the nanoparticles volume fraction, and μ_f is the base fluid dynamic viscosity, and these are the thermophysical properties of the nanoparticles. Note that

$$k_{nf}=\frac{k_s+(n-1)k_f-(n-1)\phi\left(k_f-k_s\right)}{k_s+(n-1)k_f+\phi\left(k_f-k_s\right)}k_f, \tag{7}$$

$n=3/\psi$, where ψ is called the "sphericity" which is defined as the ratio of the surface area of the sphere to that of the particle for the same volume. For spherical particles, $\psi=1$, and for the cylinders, $\psi=0.5$. This study considers the copper particle is spherical in shape, so that $n=3$, as discussed by Hamilton and Crosser [47]. The thermophysical properties of H_2O, Casson fluid, $CoFe_2O_4$, and TiO_2 are given in Table 1, following Tshivhi and Makinde [48] and Shaw et al. [49].

Equations (3)–(5) represent the nanofluid flow when $\beta\longrightarrow\infty,\phi\neq 0$ and the non-Newtonian Casson fluid flow when $\beta\neq\infty$ and $\phi=0$. The governing equations (2)–(4) are transformed into dimensionless form by introducing nondimensional variables defined as follows to obtain similar solutions:

$$u=2czf'(\eta), \\ v=-\frac{ca}{\sqrt{\eta}}f(\eta), \\ \eta=\left(\frac{r}{a}\right)^2, \\ \theta(\eta)=\frac{T-T_\infty}{T_f-T_\infty}, \tag{8}$$

where the stream function $\psi=aU_\infty/2rf(\eta)$ is related to a velocity component as follows:

$$u=\frac{\partial\psi}{\partial r}, \\ v=-\frac{\partial\psi}{\partial z}. \tag{9}$$

Since the nondimensional variables in (8) and (9) satisfy the continuity equation in (2), equations (3) and (4) are converted into the following nondimensional form:

$$A_1\left(1+\frac{1}{\beta}\right)\left[\eta f'''+f''-\frac{Re}{Da}\left(f'-1\right)\right]+Re\left[A_2\left(ff''-f'^2+1\right)-F_r\left(f'-1\right)^2\right]=0, \tag{10}$$

$$\frac{A_3}{Pr}\left(\eta\theta''+\theta'\right)+A_4Re(f\theta'-2f'\theta)+4A_1Ec\left(1+\frac{1}{\beta}\right)\left[\eta f''^2+\frac{Re}{Da}\left(f'-1\right)^2\right]+4ReEcF_r\left(f'-1\right)^3=0. \tag{11}$$

With the boundary conditions in the dimensionless form,

$$f(1)=0,f'^{(1)}=\lambda+\delta\left(1+\frac{1}{\beta}\right)f''(1),\theta'(1)=Bi[\theta(1)-1], \\ f'(\infty)\longrightarrow 1,\theta(\infty)\longrightarrow 0, \tag{12}$$

where $\eta, Da, F_r, \lambda, Re, Pr, \delta, Ec$, and Bi are the similarity variable, Darcy number (porous media parameter), Forchheimer (second order porous resistance) parameter, velocity ratio (stretching/shrinking) parameter (where $\lambda<0$ for stretching and $\lambda>0$ for shrinking of the surface), free stream Reynolds number, Prandtl number, velocity slip parameter, Eckert number, and Biot number (convective parameter), respectively. These

Table 1: Thermophysical properties of H_2O, $CoFe_2O_4$, and TiO_2 nanoparticles.

Thermophysical properties	H_2O	Casson fluid	$CoFe_2O_4$	TiO_2
Thermal conductivity, $k\ [W.m^{-1}.K^{-1}]$	0.613	0.505	3.7	8.9568
Specific heat, $C_p\ [J.kg^{-1}.K]$	4179	3490	700	686.2
Density, $\rho\ [kg.m^{-3}]$	997.1	1060	4907	4250

dimensionless parameters and the variables A_1, A_2, A_3 and A_4 quantities are defined as follows:

$$Da = \frac{2ck_1}{\nu_f}, A_1 = (1-\phi)^{-2.5}, A_2 = 1-\phi+\phi\frac{\rho_s}{\rho_f}, F_r = \frac{zF}{\rho_f\sqrt{k_1}},$$

$$Ec = \frac{U_\infty^2}{(C_p)_f(T_f - T_\infty)}, \delta = \frac{2r\mu_f}{a^2 L}, Bi = \frac{a^2 h_f}{2rk_f}, Re = \frac{a^2 c}{2\nu_f}, \lambda = \frac{b}{c}, \quad (13)$$

$$A_3 = \frac{k_s + 2k_f - 2\phi(k_f - k_s)}{k_s + 2k_f + \phi(k_f - k_s)}, Pr = \frac{\nu_f(\rho C_p)_f}{k_f}, A_4 = 1-\phi+\phi\frac{(\rho C_p)_s}{(\rho C_p)_f}.$$

Note that

(i) According to Joseph et al. [50], the pressure gradient in the flow due to porous medium ∇P is given by

$$\nabla P = -\frac{\mu}{k_1}q - \frac{C_F\rho_f}{\sqrt{k_1}}|q|q, \quad (14)$$

where q is the velocity vector, k_1 is the permeability of the porous medium (m^2), $C_F = 11/20(1 - 11/20d/D_e)$ is a dimensionless form-drag constant, d is the diameter of spheres of the porous medium, and $D_e = 2wh/w + h$ is the equivalent diameter of the bed (defined in terms of the height h and width w of the bed). Thus, putting $F \equiv \rho C_F$ (kgm^{-3}) confirms the dimensionlessness of Fr.

(ii) $Re \equiv 1/4\kappa^2$, where $\kappa = \sqrt{z\nu_f/U_\infty a^2}$ is the curvature of the cylinderical surface, as described by Gorla [24] and Alizadeh et al. [38].

3. Physical Quantities of Engineering Interest

The heat flux q_w and wall skin friction τ_w are computed as follows:

$$q_w = -k_{nf}\frac{\partial T}{\partial r}\Big|_{r=a}, \quad \tau_w = \mu_{nf}\left(1+\frac{1}{\beta}\right)\frac{\partial u}{\partial r}\Big|_{r=a}, \quad (15)$$

and thus, the physical quantities of engineering interest: the reduced local Nusselt number Nu_z and coefficient of reduced skin friction C_f are given by

$$Nu_z = \frac{zq_w}{k_f(T_f - T_\infty)}, \quad C_f = \frac{\tau_w}{\rho_f U_\infty^2}. \quad (16)$$

On simplification,

$$\frac{a}{z}Nu_z = -2A_3\theta'(1), \quad \frac{z}{a}ReC_f = \frac{A_1}{2}\left(1+\frac{1}{\beta}\right)f''(1), \quad (17)$$

where $Re = a^2c/2\nu_f$ represents Reynolds number (Gorla [24]). The heat transfer enhancement (HTE) of the $CoFe_2O_4$-H_2O and TiO_2-H_2O nanoparticles are computed using the following formula:

$$\mathrm{HTE} = \frac{Nu_z(\phi \neq 0) - Nu_z(\phi = 0)}{Nu_z(\phi = 0)} * 100. \quad (18)$$

4. Temporal Stability Analysis of the Solution

On solving problems involving boundary layer flow, the solution could be multiple, unique, or does not exist. In the case of two or more solutions, the upper branch (first) solution is given to the solution that initially satisfies the boundary condition at the far field. The temporal stability analysis has proved that the upper branch solution is the only one that is physically realizable and stable in most problems. However, according to Weidman et al. [18], there also exists a problem that has a lower branch solution that is stable. Therefore, it is necessary to execute the stability analysis and validate the reliability of the stable solutions. If an initial growth of perturbation appears in the solution, the solution is not physically realizable. The perturbation may exponentially increase or decay with time, and that is the reason for considering an unsteady (time-dependent) problem form in the stability analysis formulation. Thus, an unsteady form, Merkin [43], of equations (3) and (4) becomes

$$\frac{\partial u}{\partial t}+u\frac{\partial u}{\partial z}+v\frac{\partial u}{\partial r}=U_\infty\frac{dU_\infty}{dz}+\frac{\mu_{nf}}{\rho_{nf}}\left(1+\frac{1}{\beta}\right)\left(\frac{\partial^2 u}{\partial r^2}+\frac{1}{r}\frac{\partial u}{\partial r}\right)-\frac{\mu_{nf}}{\rho_{nf}k_1}\left(1+\frac{1}{\beta}\right)\left(u-U_\infty\right)-\frac{F}{\rho_{nf}\sqrt{k_1}}\left(u-U_\infty\right)^2, \tag{19}$$

$$\frac{\partial T}{\partial t}+u\frac{\partial T}{\partial z}+v\frac{\partial T}{\partial r}=\frac{k_{nf}}{\left(\rho c_p\right)_{nf}}\left(\frac{\partial^2 T}{\partial r^2}+\frac{1}{r}\frac{\partial T}{\partial r}\right)+\frac{\mu_{nf}}{\left(\rho c_p\right)_{nf}}\left(1+\frac{1}{\beta}\right)\left(\frac{\partial u}{\partial r}\right)^2+\frac{\mu_{nf}}{\left(\rho C_p\right)_{nf}k_1}\left(1+\frac{1}{\beta}\right)\left(u-U_\infty\right)^2+\frac{F}{\left(\rho C_p\right)_{nf}\sqrt{k_1}}\left(u-U_\infty\right)^3, \tag{20}$$

where t is time. The unsteady equations (19) and (20) are transformed as follows:

$$\begin{aligned}u&=2czf'(\eta,\tau),\\ v&=-\frac{ca}{\sqrt{\eta}}f(\eta,\tau),\\ \eta&=\left(\frac{r}{a}\right)^2,\\ \theta(\eta,\tau)&=\frac{T-T_\infty}{T_f-T_\infty},\\ \tau&=2ct,\end{aligned} \tag{21}$$

where τ represents the nondimensional time variable. Inserting (21) into equations (15) and (16), the resulting equations become

$$A_1\left(1+\frac{1}{\beta}\right)\left[\eta\frac{\partial^3 f}{\partial\eta^3}+\frac{\partial^2 f}{\partial\eta^2}-\frac{1}{Da}\left(\frac{\partial f}{\partial\eta}-1\right)\right]+A_2Re\left[f\frac{\partial^2 f}{\partial\eta^2}-\left(\frac{\partial f}{\partial\eta}\right)^2-\frac{\partial^2 f}{\partial\tau\partial\eta}+1\right]-ReF_r\left(\frac{\partial f}{\partial\eta}-1\right)^2=0, \tag{22}$$

$$\frac{A_3}{Pr}\left(\eta\frac{\partial^2\theta}{\partial\eta^2}+\frac{\partial\theta}{\partial\eta}\right)+A_4Re\left(f\frac{\partial\theta}{\partial\eta}-2\frac{\partial f}{\partial\eta}\theta-\frac{\partial\theta}{\partial\tau}\right)+4ReEcF_r\left(\frac{\partial f}{\partial\eta}-1\right)^3+4A_1Ec\left(1+\frac{1}{\beta}\right)\left[\eta\left(\frac{\partial^2 f}{\partial\eta^2}\right)^2+\frac{1}{Da}\left(\frac{\partial f}{\partial\eta}-1\right)^2\right]=0, \tag{23}$$

with the time dependent boundary conditions

$$f(1,\tau) = 0, \frac{\partial f}{\partial \eta}(1,\tau) = \lambda + \delta\left(1 + \frac{1}{\beta}\right)\frac{\partial^2 f}{\partial \eta^2}(1,\tau),$$
$$\frac{\partial \theta}{\partial \eta}(1,\tau) = -Bi[1 - \theta(1,\tau)], \frac{\partial f}{\partial \eta}(\infty,\tau) \longrightarrow 1, \theta(\infty,\tau) \longrightarrow 0. \tag{24}$$

To investigate the stability of the similarity solutions $f(\eta) = f_0(\eta)$ and $\theta(\eta) = \theta_0(\eta)$ that satisfy boundary value problems (10)–(12), the perturbation equation (25) is induced following Weidman et al. [51]. Here, $F(\eta,\tau)$ and $G(\eta,\tau)$ are small relative to $f_0(\eta)$ and $\theta_0(\eta)$, respectively, whereas an unknown eigenvalue parameter (a small disturbance of decay or growth) ε is used in the formulation, which provides an infinite set of the eigenvalues $\varepsilon_1 < \varepsilon_2 < \varepsilon_3 < \ldots$

$$\left.\begin{aligned} f(\eta,\tau) &= f_0(\eta) + e^{-\varepsilon\tau}F(\eta,\tau) \\ \theta(\eta,\tau) &= \theta_0(\eta) + e^{-\varepsilon\tau}G(\eta,\tau) \end{aligned}\right\}. \tag{25}$$

After employing (25) into (22)–(24), the following linearized eigenvalue problem is attained such that

$$\begin{aligned} &A_1\left(1 + \frac{1}{\beta}\right)\eta\frac{\partial^3 F}{\partial \eta^3} + \left[A_1\left(1 + \frac{1}{\beta}\right) + A_2 Re f_0\right]\frac{\partial^2 F}{\partial \eta^2} - A_2 Re\frac{\partial^2 F}{\partial \tau \partial \eta} \\ &+ \left[A_2 Re(\varepsilon - 2f_{0'}) - \frac{A_1}{Da}\left(1 + \frac{1}{\beta}\right) - 2ReF_r(f_{0'} - 1)\right]\frac{\partial F}{\partial \eta} + A_2 Re f_{0''}F = 0, \end{aligned} \tag{26}$$

$$\begin{aligned} &\frac{A_3}{Pr}\eta\frac{\partial^2 G}{\partial \eta^2} + \left(\frac{A_3}{Pr} + A_4 Re f_0\right)\frac{\partial G}{\partial \eta} + A_4 Re(\varepsilon - 2f_{0'})G + 8A_1 Ec\left(1 + \frac{1}{\beta}\right)f_{0''}\frac{\partial^2 F}{\partial \eta^2} \\ &+ \left[\frac{8A_1 Ec}{Da}\left(1 + \frac{1}{\beta}\right)(f_{0'} - 1) + 12\text{ReEcFr}(f_{0'} - 1)^2 - 2A_4 Re\theta_0\right]\frac{\partial F}{\partial \eta} + A_4 Re\theta_{0'}F \\ &- A_4 Re\frac{\partial G}{\partial \tau} = 0, \end{aligned} \tag{27}$$

subjected to modified the boundary conditions:

$$\begin{aligned} &F(1,\tau) = 0, \frac{\partial F}{\partial \eta}(1,\tau) = \delta\left(1 + \frac{1}{\beta}\right)\frac{\partial^2 F}{\partial \eta^2}(1,\tau), \frac{\partial G}{\partial \eta}(1,\tau) = Bi\,G(1,\tau), \\ &\frac{\partial F}{\partial \eta}(\infty,\tau) \longrightarrow 0, G(\infty,\tau) \longrightarrow 0. \end{aligned} \tag{28}$$

The initial decay or growth of the solution (25) is identified by obtaining the steady state solution taking $\tau = 0$ and hence $F = F_0(\eta)$ and $G = G_0(\eta)$ in equations (22)–(24), where $0 < F_0(\eta) \ll 1$ and $0 < G_0(\eta) \ll 1$ (Weidman et al.) [51]. The stability of the solution obtained depends on the sign of the smallest eigenvalue ε. The fact that the eigenvalue ε_1 is positive implies that the flow is real and stable and that there is an initial decay. To the contrary, the value of ε_1 is negative, which indicates that the steady flow solution is unstable and that there is an initial growth of disturbance. Now, the simplified and linearized eigenvalue problem above can be rewritten as follows:

$$A_1\left(1+\frac{1}{\beta}\right)\eta F_{0'''} + \left[A_1\left(1+\frac{1}{\beta}\right) + A_2 Re f_0\right]F_{0''} + \left[A_2 Re(\varepsilon - 2f_{0'}) - \frac{A_1}{Da}\left(1+\frac{1}{\beta}\right) - 2ReF_r(f_{0'}-1)\right]F_{0'} + A_2 Re f_{0''} F_0 = 0, \tag{29}$$

$$\frac{A_3}{Pr}\eta G_{0''} + \left(\frac{A_3}{Pr} + A_4 Re f_0\right)G_{0'} + A_4 Re(\varepsilon - 2f_{0'})G_0 + 8A_1 Ec\left(1+\frac{1}{\beta}\right)f_{0''}F_{0''} + \left[\frac{8A_1 Ec}{Da}\left(1+\frac{1}{\beta}\right)(f_{0'}-1) + 12ReEcFr(f_{0'}-1)^2 - 2A_4 Re\theta_0\right]F_{0'} + A_4 Re\theta_{0'} F_0 = 0, \tag{30}$$

subjected to the following boundary conditions:

$$F_0(1) = 0, F_{0'}(1) = \delta\left(1+\frac{1}{\beta}\right)F_{0''}(1), G_{0'}(1) = Bi\, G_0(1), \quad F_{0'}(\infty) \longrightarrow 0, G_0(\infty) \longrightarrow 0. \tag{31}$$

To find the possible range of the smallest eigenvalue ε_1, equations (25) and (26) along with the boundary conditions (31) are computed using the bvp solver functions embedded in Maple. To do this, (29) needs a modification, and hence, the BVP code can successfully execute the computation. Therefore, $F_{0'}(\infty) \longrightarrow 0$ is relaxed and substituted with a condition such as $F_{0''}(0) = 1$, following Harris et al. [25]. The modified boundary conditions in (31) becomes

$$F_0(1) = 0, F_{0'}(1) = \delta\left(1+\frac{1}{\beta}\right)F_{0''}(1), G_{0'}(1) = Bi\, G_0(1), F_{0''}(1) = 1, \quad F_{0'}(\infty) \longrightarrow 0, G_0(\infty) \longrightarrow 0. \tag{32}$$

5. Numerical Method

In order to apply the solver, the equations must be rewritten as a set of equivalent ordinary differential equations of first order. This is done using the substitutions, where $y(1) = f$ and $y(4) = \theta$ as follows:

$$\begin{aligned}
y(1)' &= f' = y(2),\\
y(2)' &= f'' = y(3),\\
y(3)' &= f''' = \frac{1}{\eta}\left\{-y(2) + \frac{Re}{Da}(y(2)-1) - \frac{Re}{A1(1+1/\beta)}\left[A2(y(1)y(3) - y(2)y(2) + 1) - Fr(1-y(2))^2\right]\right\},\\
y(4)' &= \theta' = y(5),\\
y(5)' &= \theta'' = -\frac{1}{\eta}\left\{y(5) + \frac{Pr}{A3}\left[A4Re(y(1)y(5) - 2y(2)y(4)) + 4A1Ec\left(1+\frac{1}{\beta}\right)\left[\eta y(3)y(3) + \frac{Re}{Da}(y(2)-1)^2\right] + 4ReEcFr(y(2)-1)^3\right]\right\}.
\end{aligned} \tag{33}$$

For the boundary conditions (12), we get

$$ya(1) = 0, ya(2) = \lambda + \delta\left(1 + \frac{1}{\beta}\right)k_1, ya(3) = k_1, yb(2) = 1,$$
$$ya(4) = k_2, ya(5) = Bi[k_2 - 1], yb(4) = 0. \quad (34)$$

The same procedures are followed for stability analysis. New substitutions are introduced to rewrite equations (25) and (26) and the boundary conditions (32) into first-order ordinary differential equations by letting where $y(1) = F_0$, $y(4) = G_0, z(1) = f_0$, and $z(4) = \theta_0$:

$$\begin{aligned}
y(1)' &= F_{0'} = y(2),\\
y(2)' &= F_{0''} = y(3),\\
y(3)' &= F_{0'''} = -\frac{1}{A1(1+1/\beta)\eta}\left\{\left[A1\left(1+\frac{1}{\beta}\right) + A2\mathrm{Re}z(1)\right]y(3) + \left[A2Re(\varepsilon - 2z(2))\right.\right.\\
&\quad \left.\left. -\frac{A1Re}{Da}\left(1+\frac{1}{\beta}\right) - 2\mathrm{ReFr}(z(2)-1)\right]y(2) + A2\mathrm{Re}z(3)y(1)\right\},\\
y(4)' &= G_{0'} = y(5),\\
y(5)' &= G_{0''} = -\frac{Pr}{A3\eta}\left\{\left[\frac{A3}{Pr} + A4\mathrm{Re}z(1)\right]y(5) + A4Re\left]\varepsilon - 2z(2)\right]y(4)\right.\\
&\quad + 8A1\mathrm{ReEc}\left(1+\frac{1}{\beta}\right)z(3)y(3) + \left[\frac{8A1Ec}{Da}\left(1+\frac{1}{\beta}\right)(z(2)-1)\right.\\
&\quad \left.\left. + 12\mathrm{ReEcFr}(z(2)-1)^2 - 2A4\mathrm{Re}z(4)\right]y(2) + A4\mathrm{Re}z(5)y(1)\right\}.
\end{aligned} \quad (35)$$

For the boundary conditions, we get

$$ya(1) = 0, ya(2) = \delta\left(1 + \frac{1}{\beta}\right)k_1, ya(3) = k_1, yb(2) = 0,$$
$$ya(4) = k_2, ya(5) = Bi\,k_2, ya(3) = 1, yb(4) = 0,$$
$$za(1) = 0, za(2) = \lambda + \delta\left(1 + \frac{1}{\beta}\right)l_1, za(3) = l_1, zb(2) = 1,$$
$$a(4) = l_1, za(5) = Bi[l_2 - 1], zb(4) = 0. \quad (36)$$

To determine the unknown initial conditions k_1, k_2, l_1, and l_2 (i.e., the values of $f''(1)$, $\theta(1)$, $F_0''(1)$, and $G_0(1)$, respectively), shooting the equations is performed for an arbitrary slope so that the solution of the system of ODEs satisfies the boundary conditions at ∞, and its accuracy is checked by comparing the calculated quantities with the provided end points. After obtaining these values, the fourth-fifth order Runge–Kutta–Fehlberg techniques applied to solve the system of first-order ODEs in (33) with boundary conditions (33) and determine ε from (35). To get the dual solutions, different initial approximates for the values of k_1, k_2 are considered where all profiles asymptotically satisfy the ∞ boundary conditions.

6. Results and Discussion

In this research article, the cumulative effects of the velocity ratio (stretching/shrinking) parameter λ, free stream Reynolds number Re, Casson parameter (factor) β, porous media parameter (Darcy number) Da, porous media inertial resistance parameter (Forchheimer parameter) F_r, velocity slip (slipperiness) parameter δ, Prandtl number Pr, viscous dissipation parameter (Eckert number) Ec, convective heating parameter (Biot number) Bi, and nanoparticle volume fractions ϕ, on the fluid velocity and temperature profiles, drag force, and heat transfer rate are illustrated graphically in a chart, and numerically computed results are presented in tables. The range of parameters used in this article are as follows: $0.0 \le \phi \le 0.1, 0.1 \le \beta \le 10, 1 \le Da \le 10$, $0.1 \le Fr \le 0.3, 0.5 \le Re \le 1, 0.1 \le \delta \le 0.15, 2.2 \le Pr \le 6.2, 0.1 \le Ec \le 0.3, 0.1 \le Bi \le 0.14$. Moreover, the appearance of dual solutions for some intervals of varying parameter values is explained for the coefficients of skin friction (surface drag force) $A_1/2(1+1/\beta)f''(1)$ and Nusselt number (heat transfer rate) $-2A_3\theta'(1)$ in plots and/or tables for various numerical quantities of the involving parameters. For the governing systems of highly nonlinear ordinary differential equations (9) and (10) that cannot be solved analytically, they are numerically tackled using the shooting technique with Maple 2018 (which is coded with a finite difference fourth order accuracy level and solves the boundary value problem, bvp), subjected to initial and far field boundary conditions (12). To validate this method, the computational results of (i) dimensionless stream function (f) and dimensionless temperature (θ) at $\eta = 2$, Gorla [23] and Alizadeh et al. [38] presented in Table 2, and (ii) the coefficient of skin friction, Gorla [23] and Wang [52] presented in Table 3, are compared. It is seen from the tabulated results that the comparison reveals a better agreement for each value of the dimensionless stream function, dimensionless temperature, and coefficient of skin friction. Therefore, we, the authors, are guaranteed that the method and results obtained under this study are all valid and acceptable. The velocity, temperature, local Nusselt number, and local skin friction profiles are illustrated graphically and are presented in tables.

Table 2: Comparison of values of the dimensionless stream function (f) and temperature (θ) at $\eta = 2$ for varying values of the free stream Reynolds number Re, when $\phi = Fr = \lambda = \delta = Ec = 0$, $Pr = 1.0$, and $\beta = Da = Bi = \infty$.

Re	$f(2)$			$\theta(2)$		
	[23]	[38]	Present result	[23]	[38]	Present result
0.01	0.12075	0.12051	0.1207572	0.84549	0.84557	0.8455064
0.1	0.22652	0.22659	0.2265285	0.73715	0.73701	0.7371582
1	0.46647	0.46683	0.4664705	0.46070	0.46045	0.4606932
10	0.78731	0.78725	0.7873119	0.02970	0.02983	0.0297425

Table 3: Comparison of values of skin friction $Re^{-1/2} f''(1)$ for varying values of the free stream Reynolds number Re, when $\beta = Da = \infty$ and $Fr = \phi = \lambda = \delta = 0$.

Re	[52]	[23]	Present result
0.2	1.7577	1.75770	1.75771210
1	1.484185	1.484185	1.48418510
10	1.31643	1.316427	1.31643081
100	—	1.259642	1.25964253
∞	1.232588	1.232585	1.23258819

6.1. Existence of Dual Solutions due to Shrinking Surface. For the shrinking parameter λ, the influences of varying embedded parameters on the skin friction are presented in Figures 2–5 for $CoFe_2O_4$ (CF) nanoparticle case only, and this result is compared with that of TiO_2 (TD) nanoparticle case using Table 4. Accordingly, it is revealed that dual solutions exist: the upper (solid curve) and lower (dotted curve) solution branches exist for $\lambda > \lambda_c$, and no real solution exists for $\lambda < \lambda_c$. That means, λ_c is the shrinking parameter value for the upper and lower solutions, which physically demonstrates the extent to which the surface is able to shrink while in processing. Moreover, Figures 2–5 shows that the skin friction is a decreasing function of the shrinking parameter λ for all the parameters involved in the upper branch solutions except nearer to λ_c, whereas it is purely a decreasing function for the lower branch solutions. $|\lambda_c|$ (the range of λ for which the similarity solution appears) increases with the slipperiness parameter δ and higher values of the nanoparticle volume fraction parameter ϕ, whereas it decreases with increasing values of the Casson factor β, the porous media parameter Da, porous media inertia resistance parameter Fr, and Reynolds number Re for the upper branch solutions. Beyond this critical value λ_c, no similarity solutions exist due to the boundary layer separation from the surface, which leads us to the difficulty of using boundary layer approximations to solve the problem. Furthermore, from these figures, it is observed that the upper and lower branch solutions for the coefficient of skin friction are in opposite trend except for increment in values of ϕ and δ. Comparing the graphical results with Table 4, it is revealed that the critical value λ_c is wider for TD with respect to CF nanoparticles. Figures 2(a) and 5(a) demonstrate that for the shrinking parameter λ, the coefficient of skin friction gets enhanced as the nanoparticle volume fraction ϕ increases for the upper branch solution, which could be due to the high coercivity CF. Physically, the augmentation in nanoparticle volume fraction implies that the base fluid and the nanoparticles collision raises the motion of the nanofluid, resulting in a diminishing of the momentum boundary layer thickness and increasing the drag force at the surface. It is noted that in Figures 5, 6(b), and 7, the thinner and bold curves represent upper and lower branch solutions, respectively.

The coefficient of skin friction falls as the Casson parameter β rises for the upper branch solution, as shown in Figures 2(b) and 5(a). The coefficient of skin friction is observed to drop upon improving the Casson factor β, which means that less applied force is required to move the Casson nanofluid past the surface for higher values of the Casson factor β. In other words, $\beta \longrightarrow \infty$ implies that the fluid misses its non-Newtonian properties and behaves like a Newtonian type, and hence, its velocity augments due to the reduction in the shear stress.

Figures 3(a) and 5(b) reveal that the skin friction decreases as the porous media parameter (Darcy number Da) gets higher for the upper branch solution. Again, the skin friction drops as the porous media inertial parameter Fr rises for the upper branch solution, whereas the solution interval reduced, as illustrated in Figures 3(b) and 5(b).

As demonstrated in Figures 4(a) and 5(b), the coefficient of skin friction drops with an increment in the values of Reynolds number Re for the upper branch solution. The skin friction (surface drag force) diminishes with a rise in the values of the slipperiness parameter δ, as illustrated in Figures 4(b) and 5(b) for the upper branch solution.

Generally, the above results are observed nearer to the critical shrinking parameter λ_c values, as illustrated by the plots; the computed results from Tables 4 and 5 support what is discussed above. From Table 6, far from λ_c (say at $\lambda = -0.1$), it is revealed that coefficient of the skin friction increases only with rising values of phi and Re but drops with other parameters. Moreover, it is observable that the skin friction (surface drag force) coefficient is higher for CF compared to TD near the critical λ_c, as it is observed from Table 5.

6.2. Rate of Heat Transfer. Figures 6–11 and Table 5 explain the effects of all the parameters under discussion on the heat transfer rate (local Nusselt number Nu). It is noted from the model that the energy and momentum equations are coupled, and hence, the Nusselt number characterizes a dual solution for $\lambda_c < \lambda < 0$ for the case of shrinking surfaces.

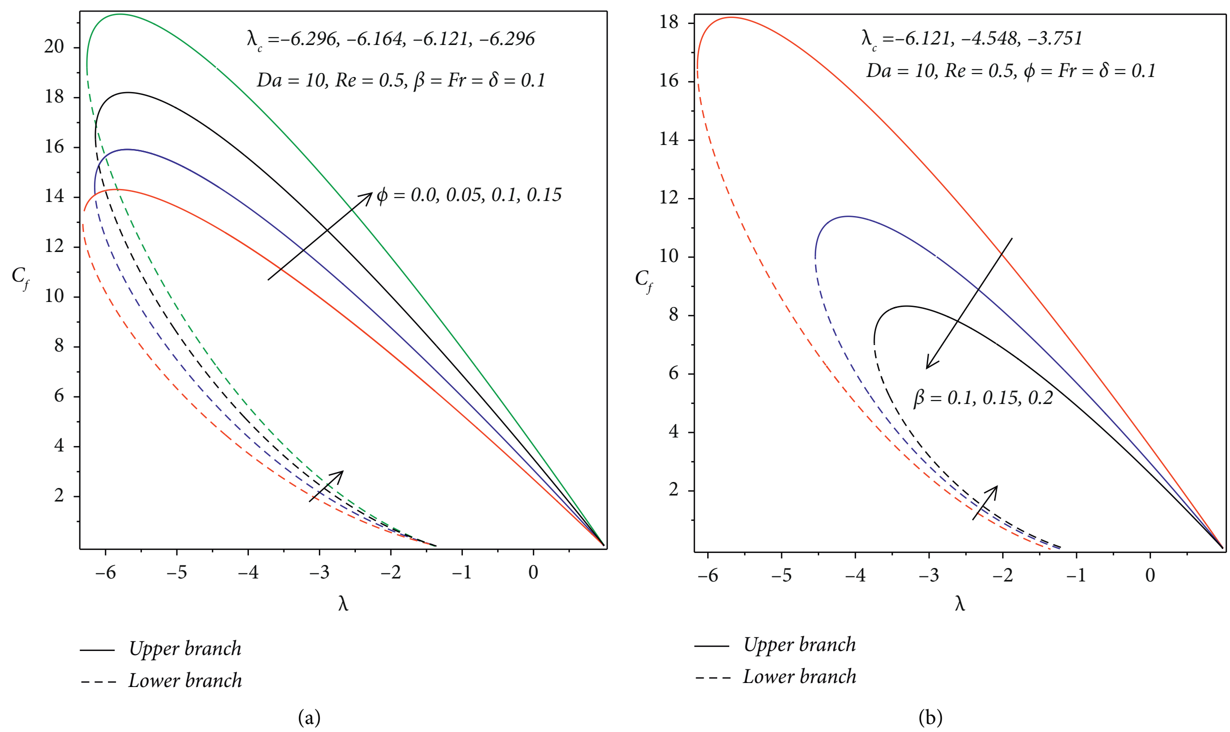

Figure 2: λ against skin friction for varying values of (a) ϕ and (b) β.

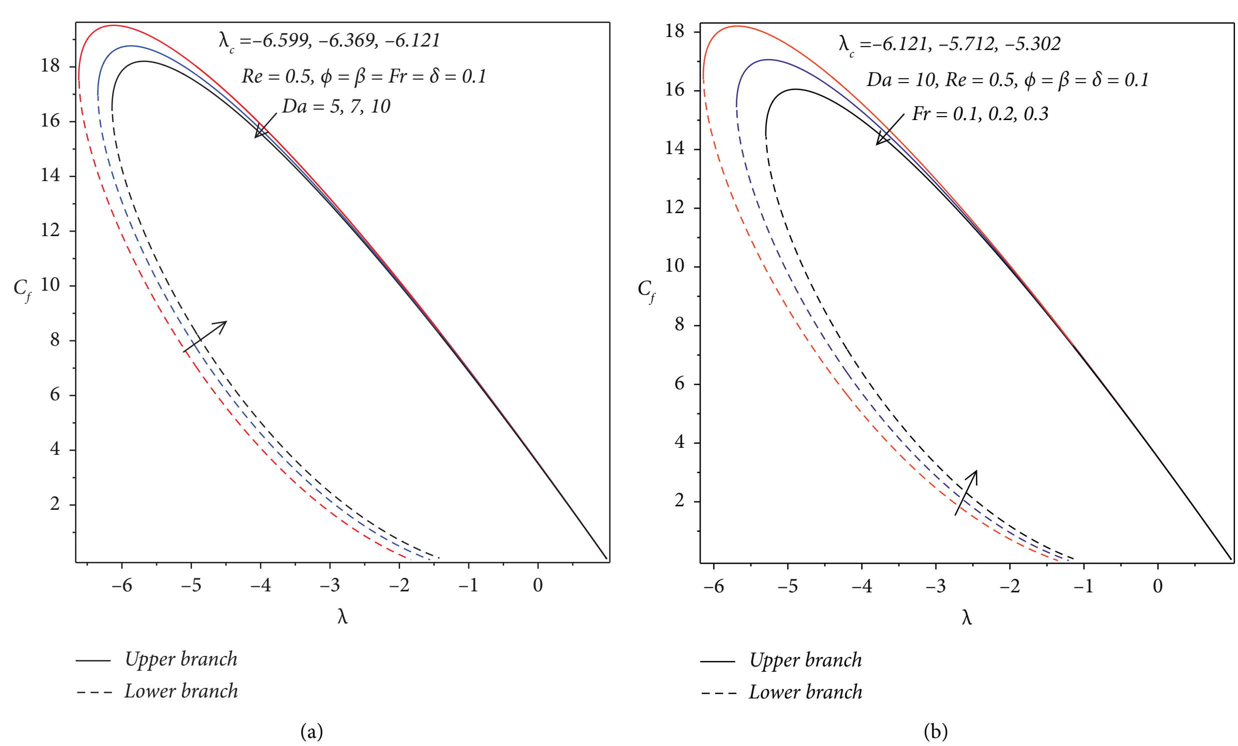

Figure 3: λ against skin friction for varying values of (a) Da and (b) Fr.

Moreover, it is revealed that dual solutions exist and that the upper branch solutions (represented by the solid curve) for the Nusselt number are an increasing function of the shrinking parameter λ, whereas the opposite trend is observed for the lower branch solutions. The critical shrinking parameter $|\lambda_c|$ for the solution decreases for increasing values of nanoparticle volume fraction, porous media inertia parameter, and Biot numbers, whereas for the

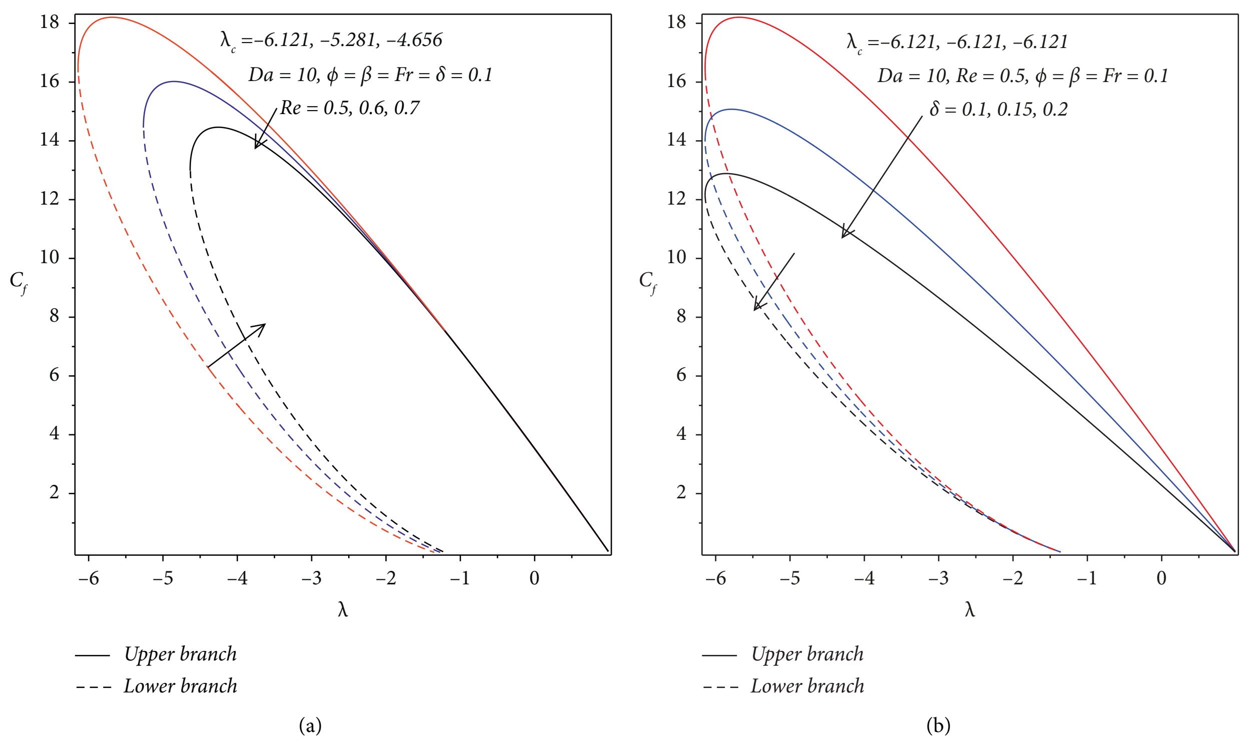

FIGURE 4: λ against skin friction for varying values of (a) Re and (b) δ.

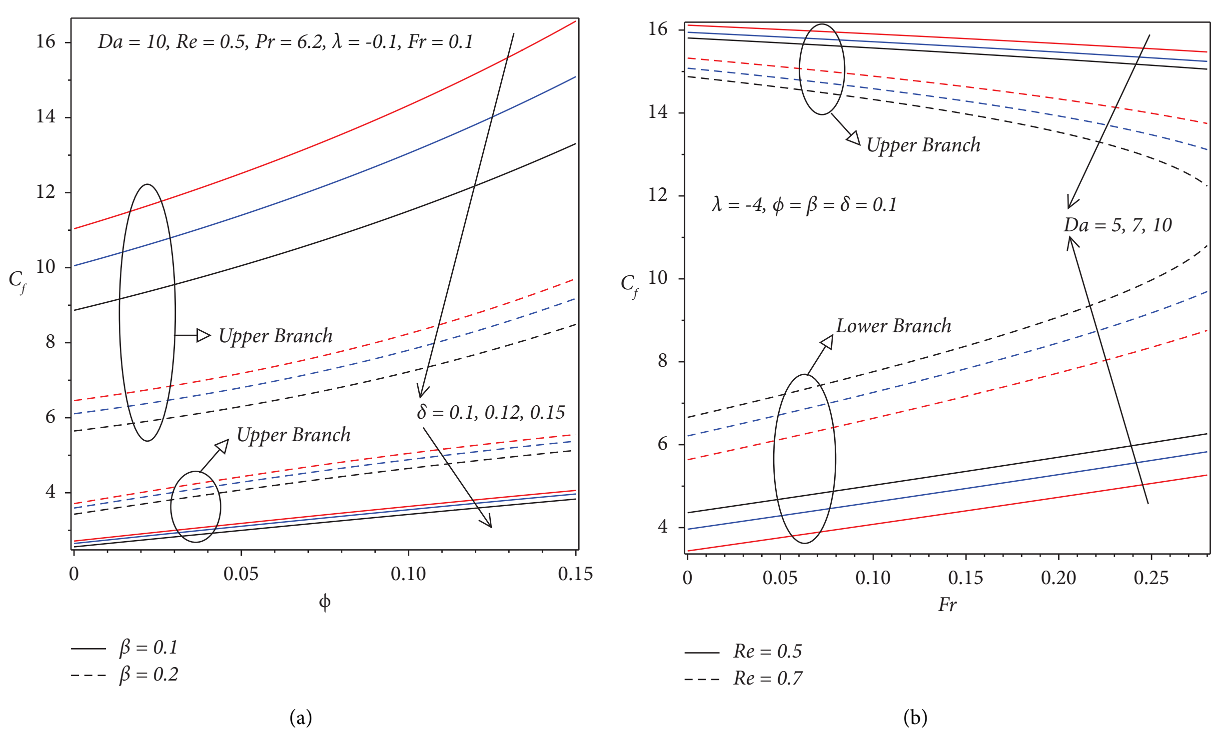

FIGURE 5: (a) ϕ, β, and δ and (b) Da, Fr, and Re against skin friction.

Casson, Reynolds, slipperiness, and velocity ratio parameters, Darcy, Prandtl, and Eckert numbers, it gets widened for the upper branch solutions.

It is observable that rising values of nanoparticle volume fraction ϕ resulted in an ascending heat transfer rate (Nusselt number Nu) for the upper branch solution, as seen in

Table 4: The computational results of critical shrinking parameter and skin friction for varying values of parameters for both upper branch (UB) and lower branch (LB) solutions, where the universal results on the 3rd row is computed for $Da = 10, Re = 0.5, \phi = \beta = Fr = \delta = 0.1$ for $CoFe_2O_4$ and TiO_2 nanoparticles application.

	Values	$CoFe_2O_4$ nanoparticle case				TiO_2 nanoparticle case			
		Shrinking parameter		Skin friction, $z/aReC_f$		Shrinking parameter		Skin friction, $z/aReC_f$	
		λ_c	λ	LB	UB	λ_c	λ	LB	UB
φ	0.0	−6.296	−6.291	7.804424	13.41113	−6.296	−6.291	7.441272	13.41113
	0.05	−6.163	−6.160	8.751245	14.71521	−6.291	−6.287	8.589124	14.79627
Da	5	−6.599	−6.594	9.824713	18.23317	−6.858	−6.853	10.88821	18.54962
	7	−6.369	−6.364	9.973547	17.17354	−6.597	−6.594	10.77125	17.79559
		−6.121	−6.117	10.08922	17.06109	−6.358	−6.353	10.398941	17.39894
β	0.15	−4.548	−4.544	5.432811	10.35182	−4.733	−4.730	6.055124	10.41189
	0.2	−3.751	−3.747	4.017591	7.557561	−3.887	−3.883	4.002217	7.609331
Fr	0.2	−5.712	−5.708	8.421154	15.75589	−5.913	−5.910	10.00817	16.10817
	0.3	−5.302	−5.298	7.798566	14.99881	−5.490	−5.486	8.507728	15.19526
Re	0.6	−5.281	−5.278	8.672531	14.76315	−5.467	−5.462	8.009925	15.30241
	0.7	−4.656	−4.652	7.121718	13.30115	−4.822	−4.817	7.553292	13.63655
δ	0.15	−6.121	−6.117	8.500941	14.44912	−6.358	−6.353	8.522848	14.71149
	0.2	−6.121	−6.117	7.298143	12.41321	−6.358	−6.353	7.811162	12.72238

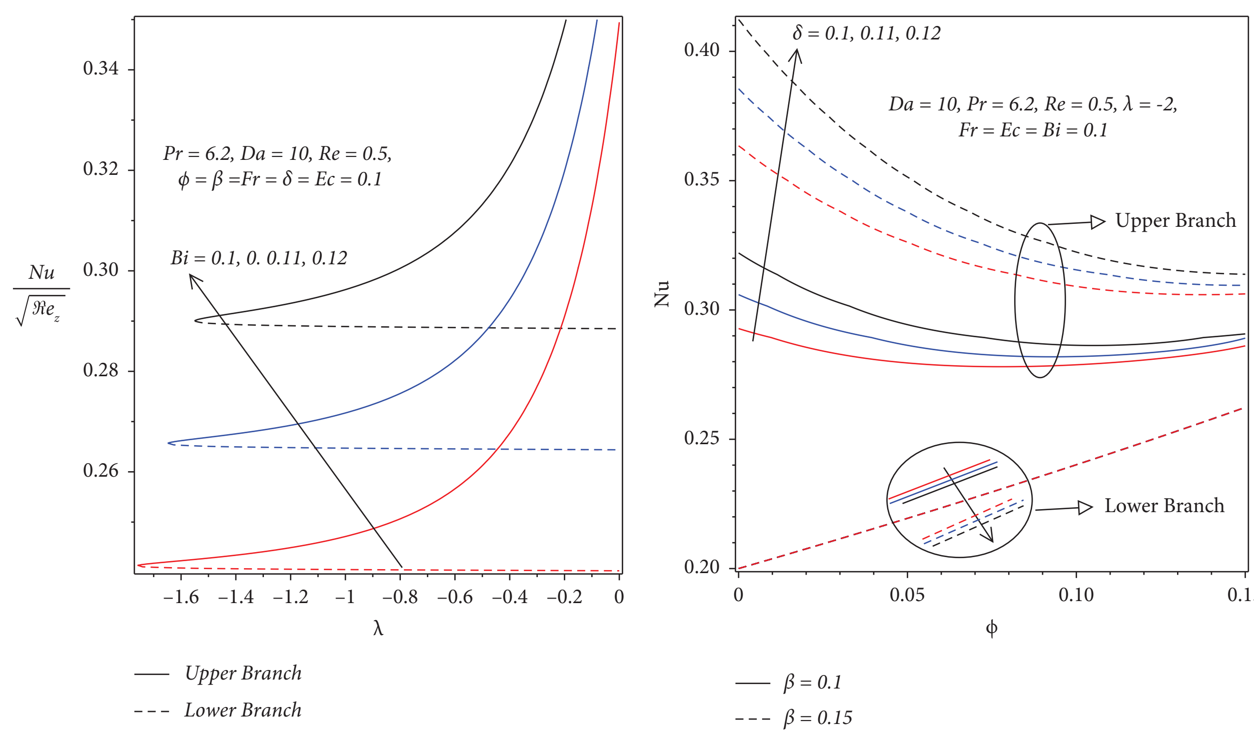

(a) (b)

Figure 6: (a) λ against Nusselt number with varying Bi. (b) ϕ, β, and δ against Nusselt number.

Figures 6(b) and 8(a) nearer to the critical shrinking parameter λ_c.

Figures 6(b) and 8(b) reveal that the augmentation in the values of the Casson factor β produces an intensified heat transfer rate nearer to the critical shrinking parameter values for the upper branch solution. Physically, an increment in the Casson factor augments the fluid motion and the thermal profile, resulting in an increase in the heat transfer rate. As $\beta \longrightarrow \infty$ (the Newtonian fluid case), the heat transfer rate is highly reduced compared to the non-Newtonian Casson fluid.

Figures 7(a) and 9 demonstrate that the intensification in the values of porous media parameter Da and porous inertia resistance parameter Fr resulted in the dropping of the heat transfer rate for the upper branch solutions nearer to the critical shrinking parameter λ_c due to the effect of the porous media against the flow rate. For the upper branch solution, nearer to

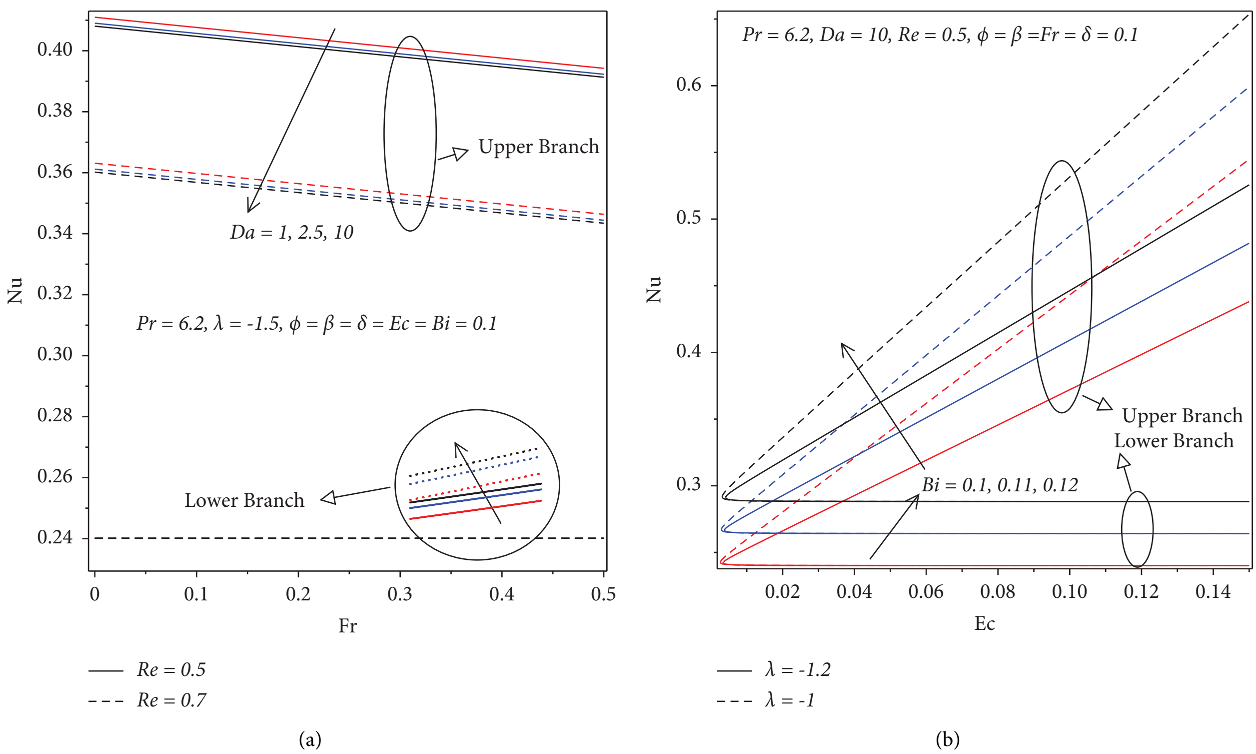

Figure 7: (a) Da, Fr, and Re and (b) Ec, Bi, and λ against Nusselt number.

Table 5: The computational results for critical shrinking parameter and the smallest eigenvalues ε of both upper branch (UB) and lower branch (LB) solutions, where the universal results on the 3rd row is computed for $Da = 10, Re = 0.5, \phi = \beta = Fr = \delta = 0.1$ for $CoFe_2O_4$ and TiO_2 nanoparticles application.

	Values	$CoFe_2O_4$ nanoparticle case				TiO_2 nanoparticle case			
		Shrinking parameter		Eigenvalue ε		Shrinking parameter		Eigenvalue ε	
		λ_c	λ	LB	UB	λ_c	λ	UB	LB
φ	0.0	−6.296	−6.291	−0.433091	4.128013	−6.337	−6.333	−0.889731	4.241711
	0.05	−6.163	−6.160	−0.454080	3.850957	−6.291	−6.287	−0.725491	3.715033
Da	5	−6.599	−6.594	−0.573897	4.644802	−6.858	−6.853	−0.048141	4.671653
	7	−6.369	−6.364	−0.533424	3.956016	−6.597	−6.594	−0.170224	4.156063
		−6.121	−6.117	−0.335706	3.909736	−6.358	−6.353	−0.365095	3.937407
β	0.15	−6.121	−6.117	−0.335706	3.909736	−6.358	−6.353	−0.365095	3.937407
	0.2	−3.751	−3.747	−0.171095	1.350239	−3.887	−3.883	−0.319463	2.738349
Fr	0.2	−5.712	−5.708	−1.096991	3.821874	−5.913	−5.910	−0.067453	3.898320
	0.3	−5.302	−5.298	−1.030511	4.037972	−5.490	−5.486	−0.663476	4.042332
Re	0.6	−5.281	−5.278	−0.309304	3.469464	−5.467	−5.462	−0.991754	3.650911
	0.7	−4.656	−4.652	−0.637060	3.288788	−4.822	−4.817	−0.478861	3.375309
δ	0.15	−6.121	−6.117	−0.773934	3.939137	−6.358	−6.353	−1.050795	3.932585
	0.2	−6.121	−6.117	−1.068120	3.973537	−6.358	−6.353	−0.811844	4.019688

Table 6: The computational results velocity profile, skin friction, temperature profile, and the Nusselt number for varying values of parameters, where the universal results on the 5th row is computed for $Da = 10, Re = 0.5, \lambda = -0.08, Pr = 6.2, \phi = \beta = Fr = \delta = Ec = Bi = 0.1$ for both $CoFe_2O_4$ and TiO_2 nanoparticles.

Parameters		$CoFe_2O_4$ nanoparticle				TiO_2 nanoparticle			
Names	Values	$f'(1)$	$z/a\mathrm{ReC}_f$	$\theta(1)$	a/zNu_z	$f'(1)$	$z/a\mathrm{ReC}_f$	$\theta(1)$	a/zNu_z
ϕ	0.0	0.3443	2.1214179	0.7885156	0.0422969	0.3443	2.1214179	0.7885156	0.0422969
	0.05	0.3470	2.4273017	0.8733792	0.0277817	0.3456	2.4190332	0.8690478	0.0295468
Pr	2.2	0.3480	2.7850414	0.6941179	0.0734467	0.3455	2.7685602	0.6854795	0.0797462

Table 6: Continued.

Parameters		CoFe$_2$O$_4$ nanoparticle				TiO$_2$ nanoparticle			
Names	Values	$f'(1)$	$z/a\mathrm{Re}C_f$	$\theta(1)$	a/zNu_z	$f'(1)$	$z/a\mathrm{Re}C_f$	$\theta(1)$	a/zNu_z
	4.2	0.3480	2.7850414	0.8611957	0.0333289	0.3455	2.7685602	0.8517387	0.0375914
Ec	0.08	0.3480	2.7850414	0.7882636	0.0508410	0.3455	2.7685602	0.7809155	0.0555485
	0.09	0.3480	2.7850414	0.8805976	0.0286702	0.3455	2.7685602	0.8721518	0.0324157
		0.3480	2.7850414	0.9729317	0.0064995	0.3455	2.7685602	0.9633880	0.0092829
β	0.15	0.2755	2.3130649	0.9932522	0.0016203	0.2727	2.2949169	0.9799335	0.0050878
	0.2	0.2316	2.0275647	0.9866240	0.0032118	0.2287	2.0088823	0.9708014	0.0074033
	1	0.0881	1.0935478	0.8090054	0.0458605	0.0856	1.0774762	0.7871929	0.0539569
Da	12	0.3432	2.7538371	0.9515903	0.0116239	0.3406	2.7367457	0.9419657	0.0147145
	15	0.3382	2.7213940	0.9289476	0.0170607	0.3355	2.7036478	0.9192120	0.0204837
Fr	0.2	0.3473	2.7800302	0.9688303	0.0074843	0.3447	2.7634303	0.9592648	0.0103283
	0.3	0.3465	2.7749759	0.9646787	0.0084812	0.3439	2.7582552	0.9550899	0.0113869
Re	0.6	0.3632	2.8840611	0.8886610	0.0267341	0.3605	2.8663237	0.8807833	0.0302272
	0.7	0.3769	2.9729610	0.8217108	0.0428098	0.3740	2.9542409	0.8151097	0.0468786
δ	0.12	0.3972	2.5874533	0.8004842	0.0479066	0.3945	2.5731069	0.7940280	0.0522239
	0.14	0.4396	2.4151383	0.6721195	0.0787288	0.4369	2.4025556	0.6677003	0.0842540
λ	0	0.3975	2.5862853	0.7995491	0.0481311	0.3951	2.5708519	0.7922350	0.0526785
	0.08	0.4467	2.3862249	0.6523665	0.0834718	0.4445	2.3718715	0.6468595	0.0895382
Bi	0.11	0.3480	2.7850414	0.9730653	0.0071142	0.3455	2.7685602	0.9635739	0.0101594
	0.12	0.3480	2.7850414	0.9731975	0.0077228	0.3455	2.7685602	0.9637579	0.0110270

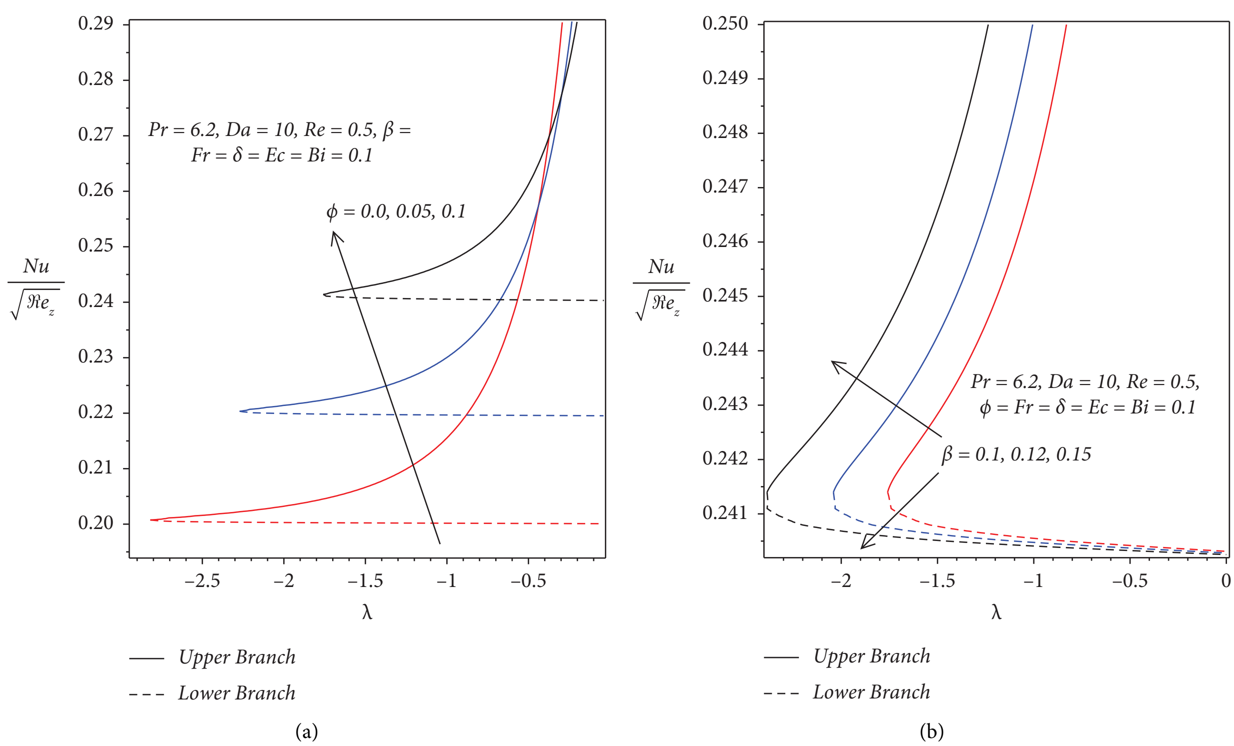

Figure 8: λ against Nusselt number with varying (a) ϕ and (b) β.

the critical shrinking parameter λ_c, increment in Reynolds number Re drops the convective heat transfer rate, as demonstrated in Figures 7(a) and 10(a). Physically, the added nanoparticles increases viscosity (Figure 2(a)), producing dominated inertial forces nearer to λ_c. Moreover, the retarded flow rate at this region leads to the overcoming of conductive heat transfer to the convective one due to better thermal conductivity of the used nanoparticles than the normal base fluid, and therefore, weak temperature gradient (Nusselt number) is observed, resulting in reduced heat transfer rate of the Casson Nanofluid flow.

Stepping up in the values of the slip parameter δ enhances the convective heat transfer rate (Nusselt number Nu) in the upper branch solution as we see from Figures 6(b) and 10(b), nearer to the critical shrinking parameter λ_c

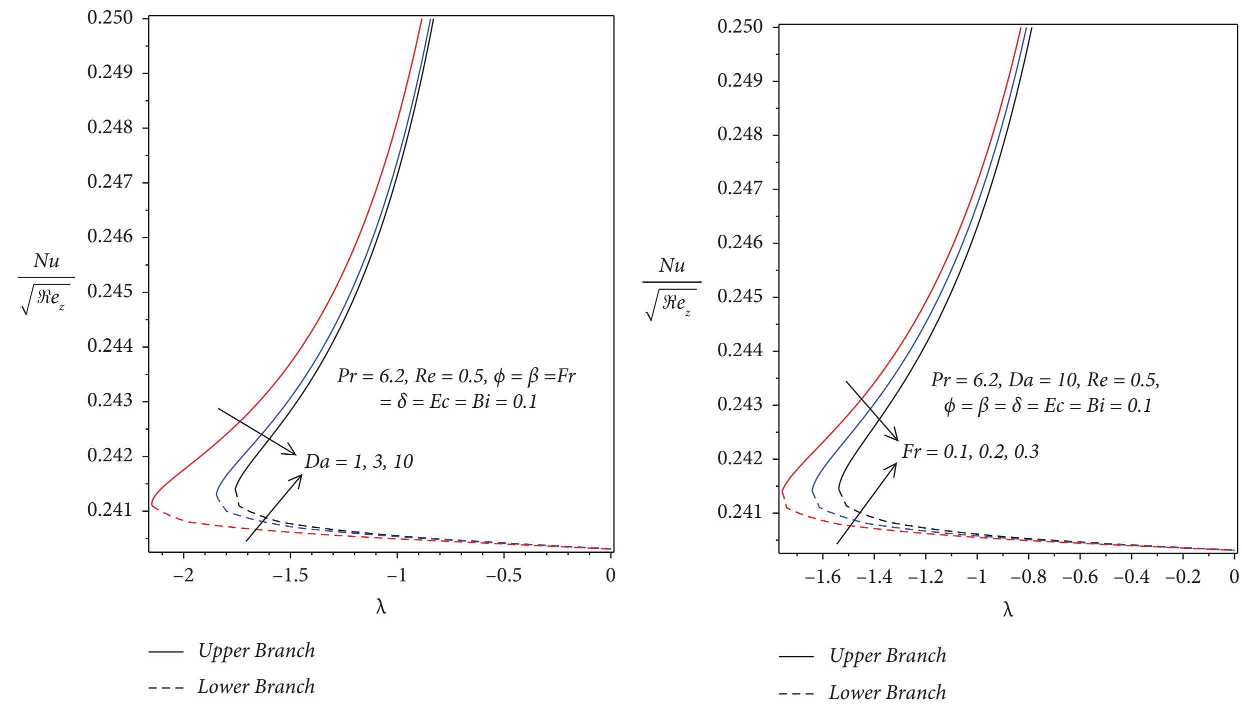

(a) (b)

FIGURE 9: λ against Nusselt number with varying (a) Da and (b) Fr.

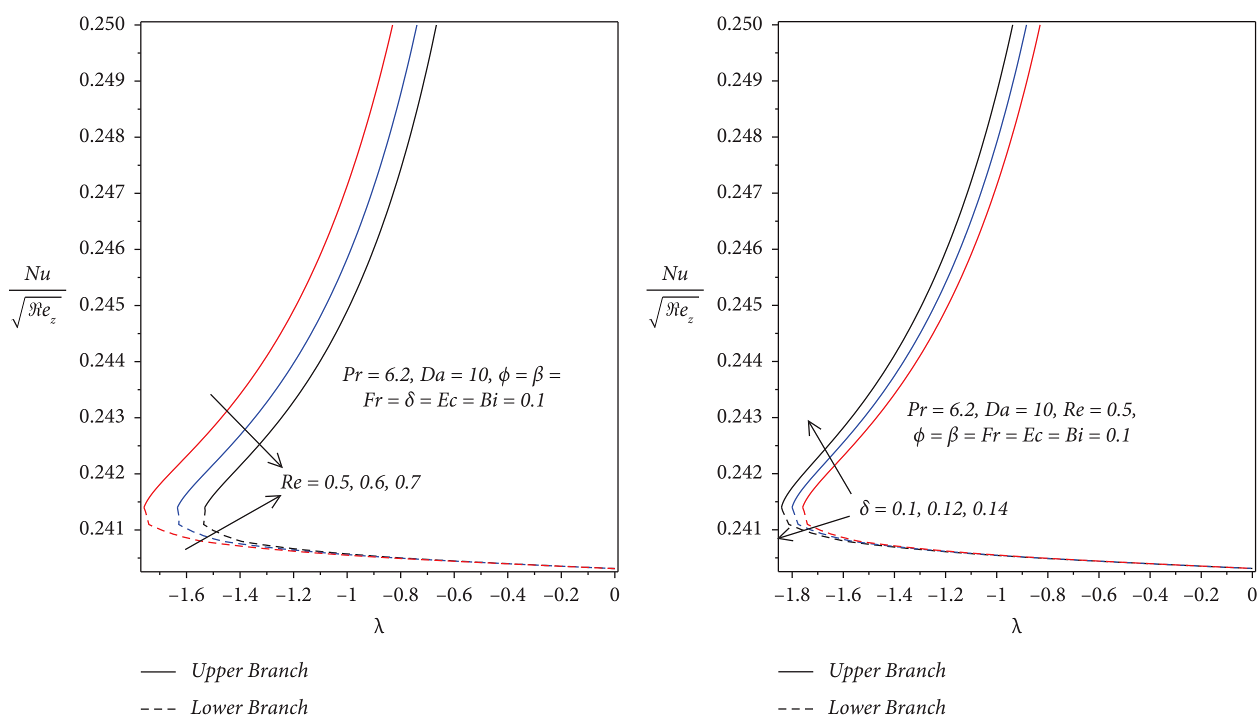

(a) (b)

FIGURE 10: λ against Nusselt number with varying (a) Re and (b) δ.

values. Physically, heat transfer rate increases as a result of an improvement in the slipperiness of the cylindrical surface, reducing adhesion of the nanofluid to it.

Figure 11(a) shows that as the Pradntl number Pr increases, the convective heat transfer rate gets higher in the upper branch solution nearer to the critical shrinking

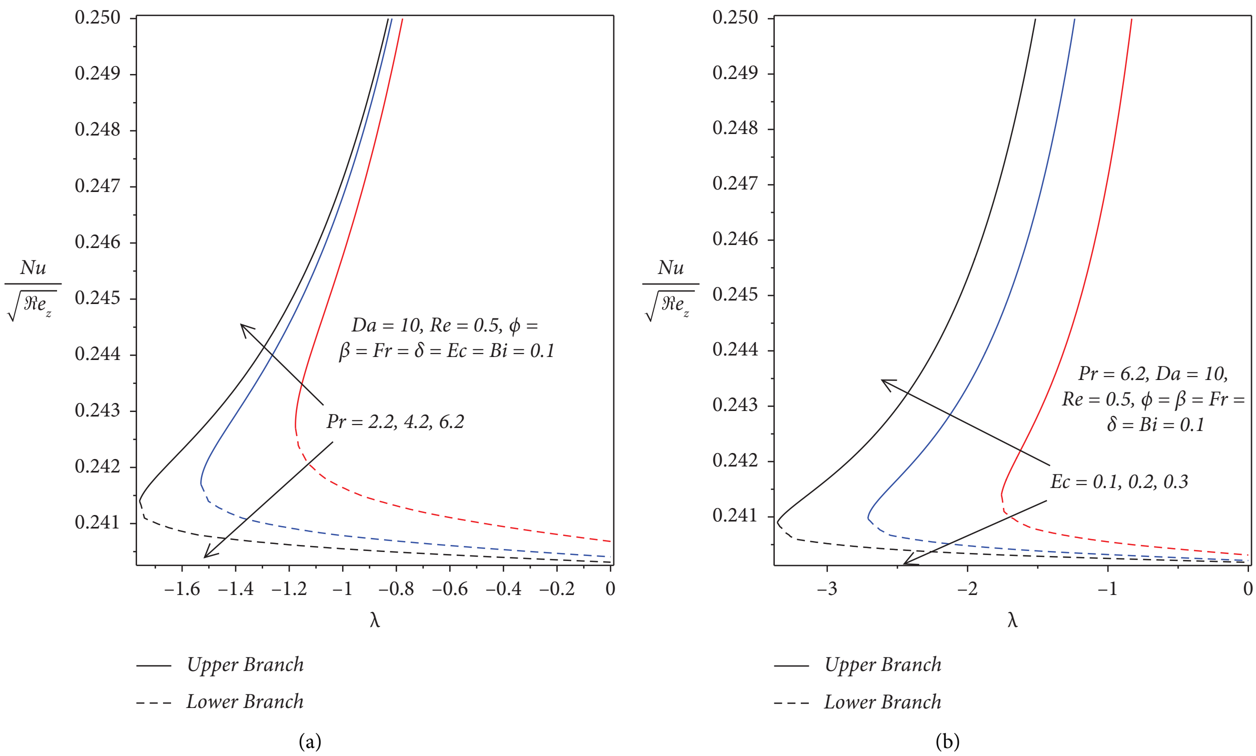

FIGURE 11: λ against Nusselt number with varying (a) Pr and (b) Ec.

parameter λ_c values. Physically, this is due to an increment in Pr, which signifies that the momentum diffuses more quickly and the velocity boundary layer is less thick than the thermal boundary layer of the fluid, meaning more heat transfer by convection is dominant in the Casson nonofluid flow.

Figures 7(b) and 11(b) illustrate as the viscous dissipation parameter Ec increases, the local Nusselt number (heat transfer rate) also increases nearer to the critical shrinking λ_c values for the upper branch solution. Figures 6(a) and 7(b) demonstrate the heat transfer rate (local Nusselt number Nu_z) against the Biot number Bi, and as it can be observed, the heat transfer rate Nu_z is increasing as the convective heating parameter (Biot number Bi) increases for the upper branch solution nearer to the critical shrinking λ_c values. Physically, it means that the coefficient of heat transfer caused by the hot fluid beneath the sheet is directly associated with the convective heating parameter. Moreover, from Figure 7(b), it is demonstrated that the heat transfer rate (Nu) escalates as the values of the shrinking parameter λ increases for the upper branch solution.

Generally, it is observed from the graphs and Table 6 that the heat transfer rate (the Nusselt number) is more pronounced for TD compared to CF nanoparticles. Moreover, nearer to λ_c, heat transfer rate (Nusselt number) increases for rising values of β, Pr, and Ec but decreases for higher values of Fr and Bi; however, the opposite trend holds far from λ_c (say at $\lambda = -0.08$).

6.3. Numerical Analysis of the Stability Test. From the numerical results of this problem, the dual solution exists for some interval of λ. The stability analysis is made to determine stable solutions within different solutions that arise due to shrinking cylindrical surfaces. As detailed in Table 5, for varying values of involving parameters, the smallest eigenvalue ε is calculated for the temporary change of small disturbances/perturbations regarding the basic steady flow, with respect to the fixed values of $Da = 10, Re = 0.5$, $\phi = \beta = Fr = \delta = 0.1$. From the table, it is observed that corresponding to the upper branch solutions, the smallest eigenvalue ε obtained is positive for shrinking surfaces, implicating that the upper branch solution is hydrodynamically temporally stable and therefore physically realizable. Clearly, for the lower branch solution, the negative value of ε revealed that it is unstable and physically unachievable. In addition, $\varepsilon > 0$ demonstrates the rate of declination of small disturbances on the upper branch solution, whereas $\varepsilon < 0$ for the lower branch solution shows the enhancement of the disturbances.

6.4. Velocity Profile. Figures 12–13(a) demonstrate the effects of different values of the embedded parameters on the fluid flow velocity profile in the case of CF nanoparticles for the UB (which is the only stable and physically realizable one) and LB (unstable and cannot be realized) solutions nearer to the critical shrinking λ_c values. In all plots, it is demonstrated that the upper and lower branch solutions are

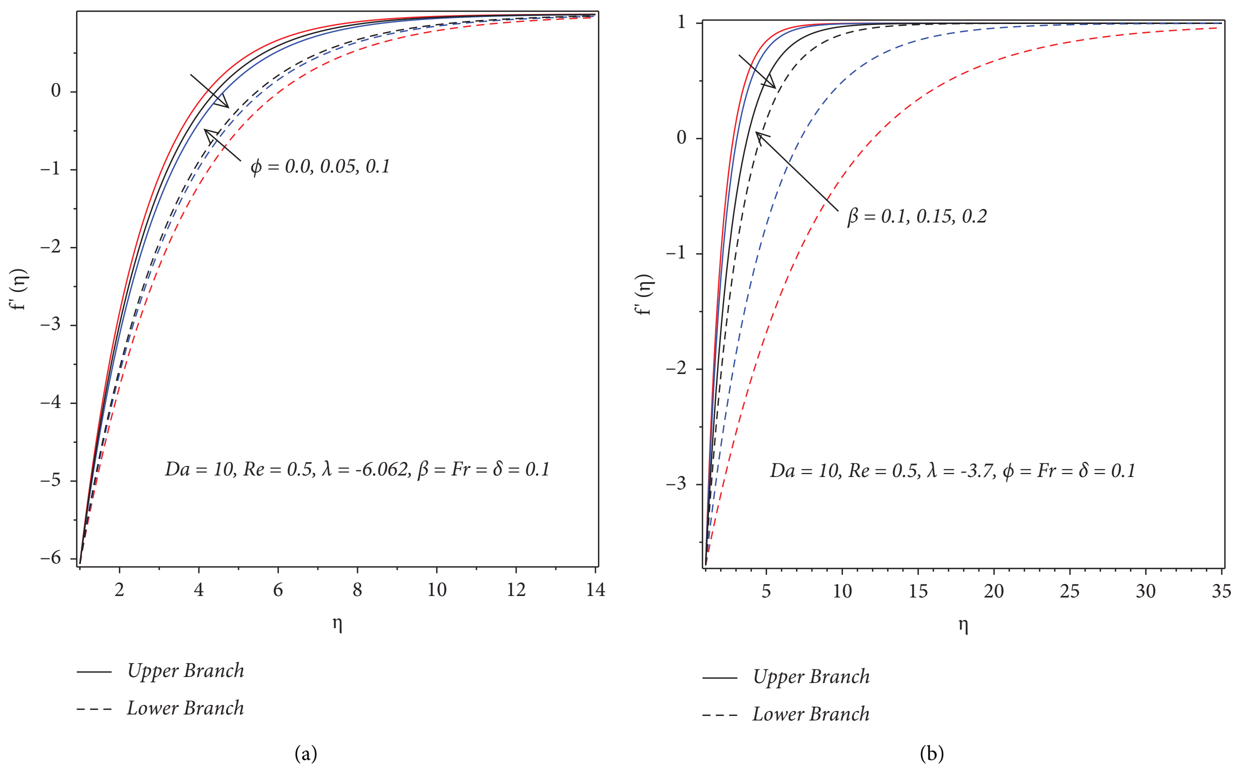

FIGURE 12: Velocity profile for shrinking parameter with (a) ϕ and (b) β.

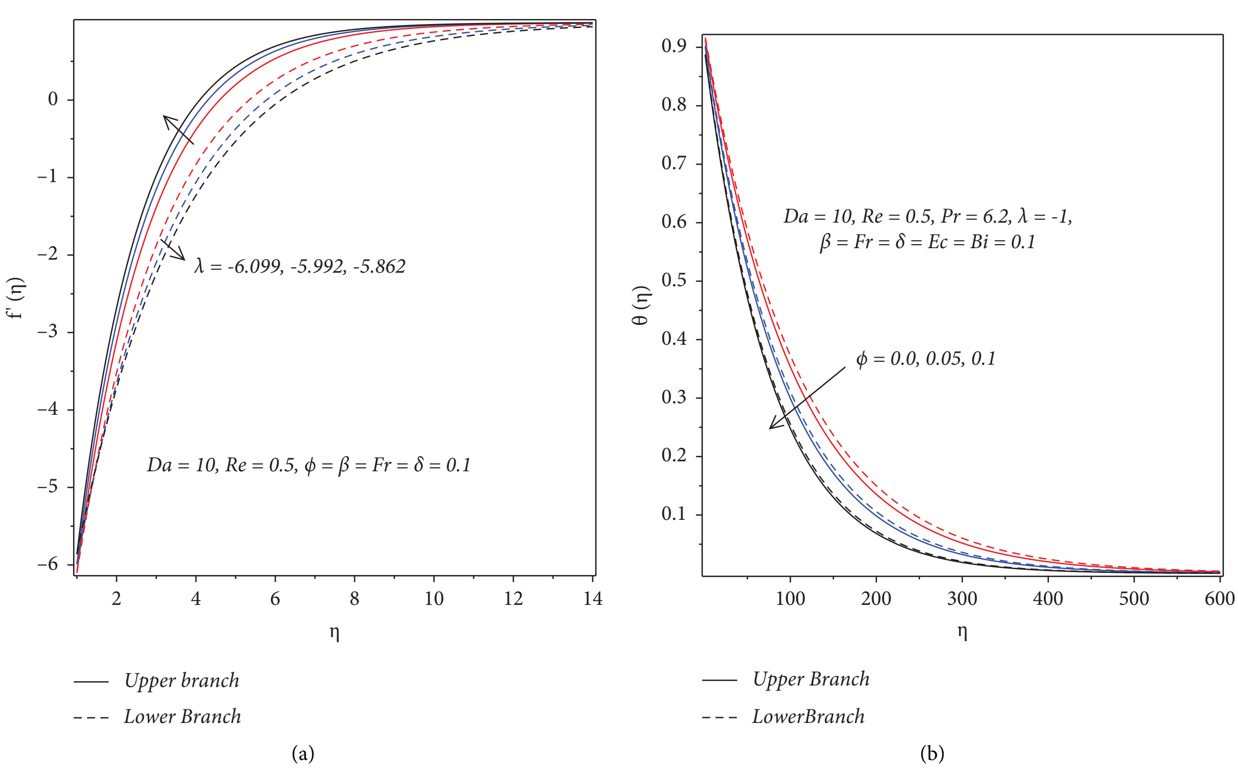

FIGURE 13: (a) Velocity profile for shrinking parameter with λ. (b) Temperature profile for shrinking parameter with ϕ.

in opposite trend. Moreover, the velocity profile is an increasing function of η, whereas for all rising values of ϕ, β, Da, Fr, Re, and δ, the velocity profile is decreasing with raising of its momentum boundary layer thicknesses nearer to $|\lambda_c|$ in the upper branch solutions. Furthermore, Fr, EC, and Bi do not have observable effect on the velocity profile and coefficient of the skin friction as Table 6, and no plot is demonstrated in this regard.

The influence of CF nanopartile volume fraction ϕ on the flow velocity profile is displayed in Figure 12(a), and it is observed that the velocity profile drops and the flow boundary layer thickness increases with enhancing nanopartile volume fraction ϕ for the upper branch solution nearer to $|\lambda_c|$, and the lower branch solution drops. Figure 12(b) depicts the influence of the Casson factor β on the fluid velocity profile, and it is observed that the velocity profile decreases with rising boundary layer thickness as the values of β augment for both the upper branch solutions. That is, the velocity of Casson nanofluid flow gets diminished when β increases, which might be due to the inverse proportionality of the Casson factor to plastic viscosity. The Newtonian fluid case happened as β got higher ($\beta \longrightarrow \infty$), and it is observed that the velocity of the Newtonian fluid is lower than that of the Casson nanofluid with widened boundary layer thicknesses.

The diminishing velocity profiles and increasing boundary layer thicknesses are observed for the rising porous media parameter Da which could be due to the influence of the application of the nanoparticles into the Casson fluid and porous matrix resistance force, which will retard flow, as demonstrated in Figure 14(a) within the flow regimes of the Casson nanofluid for both the upper branch solutions. Similarly, from Figure 14(b), it is observed that the dropping of velocity profiles for rising in porous media inertial resistance parameter Fr for the upper branch solutions with increasing boundary layer thickness. The impacts of Reynolds number Re (which measures the ratio of momentum/inertia to viscous forces) on the velocity profile are illustrated in Figure 15(a), and it is seen that as Re increases, the velocity profile drops nearer to the critical shrinking parameter value λ_c as with rising boundary layer thickness for the upper branch solutions; however, the velocity profile rises for lower branch solution. Figure 15(b) shows that as the slipperiness parameter δ increases, the velocity profile decreases with increasing boundary layer thickness for both the upper and lower branch solutions. Moreover, Figures 13(a) and 15(b) show that as the values of the velocity ratio parameter λ increases, the velocity profile increases and its boundary layer thickness diminishes in both upper and lower branch solutions.

To generalize, it is observable from the graphs under this subsection and Table 6 that the velocity profile is higher for CF compared to TD in the case of the upper branch solution at the surface of flow. Moreover, for the shrinking surface case, unlike nearer to λ_c where the velocity profile decreases with all parameters, except for λ, Table 6 reveals that far from λ_c (say at $\lambda = -0.08$), the velocity profile increases for rising values of ϕ, Da, Re, δ, and λ for the upper branch solution. Furthermore, fluctuating values of Pr, Ec, and Bi showed unobservant effects on the velocity profile and its boundary layer thickness and the skin friction coefficient, perhaps due to dominance in the thermal diffusivity, energy, and resistance for convection at the cylindrical surface of the Casson nanofluid in the upper branch solutions.

6.5. Temperature Profile. The overall impacts of varying values of the involving parameters on the fluid temperature profile and related boundary layer thickness for the shrinking parameter λ are demonstrated in Figures 13(b)–16. It is observed from the plots that the temperature profile is a decreasing function of η for all parameters under consideration nearer to λ_c. The upper and lower branch solutions are in opposite trend except for the parameters ϕ and Bi.

The temperature profile behavior in dealing with different values of nanoparticle volume fraction ϕ is illustrated in Figure 13(b), and it is observed that the temperature profile and its boundary layer thickness diminishes for increasing ϕ in both upper and lower branch solutions. Physically, increasing the nanoparticle volume fraction ϕ raises the thermal conductivity of the fluid, and hence, intensifies the temperature gradient of the Casson nanofluid, and drops the thermal behavior of the Casson nanofluid flow.

From Figure 17(a), it is observed that the temperature profile and the corresponding boundary layer thickness diminish with increasing values of the Casson factor β for the upper branch solution. Physically, when the Casson factor values become higher, the strength of the yield stress of the Casson fluid is weakened, enhancing the plastic dynamic viscosity and therefore diminishing the thickness of the thermal boundary layer of the flow temperature profile. Note that the Casson nanofluid's thermal boundary layer thickness is higher than that of the Newtonian fluid. The values of the Casson parameter get higher ($\beta \longrightarrow \infty$) which shows weaker interactions of molecular motion within the Casson nanofluid behaving as a Newtonian Casson fluid, which ultimately reduces the Casson nanofluid's temperature profile.

Figure 17(b) shows that the temperature profile and its boundary layer thickness rises against the increment in Da within the flow regime for the upper branch solution. Physically, the increment in porous matrix reduces the temperature gradient and hence enhances the thermal properties of the Casson nanofluid flow. Moreover, from Figure 18(a), it is observed that the temperature profile and its boundary layer thickness rises against the increment in the values of Fr for the upper branch solution.

Figure 18(b) reveals that rising values of Reynolds number Re resulted in an intensification of the temperature profile and its thermal boundary layer thickness for the upper branch solutions. Physically, it indicates that as Reynolds number Re rises, the temperature gradient drops due to dominance in thermal conductivity, and hence, the temperature of the fluid starts to rise. In Figure 19(a), it is demonstrated that an increment in the slipperiness parameter δ resulted in the dropping of the temperature profile and its thermal boundary layer thickness for the upper branch solution. Physically, the slipperiness of the surface facilitates the temperature gradient, resulting in a reduction of the temperature profile and a lessening of the corresponding thermal boundary layer thickness of the Casson nanofluid flow.

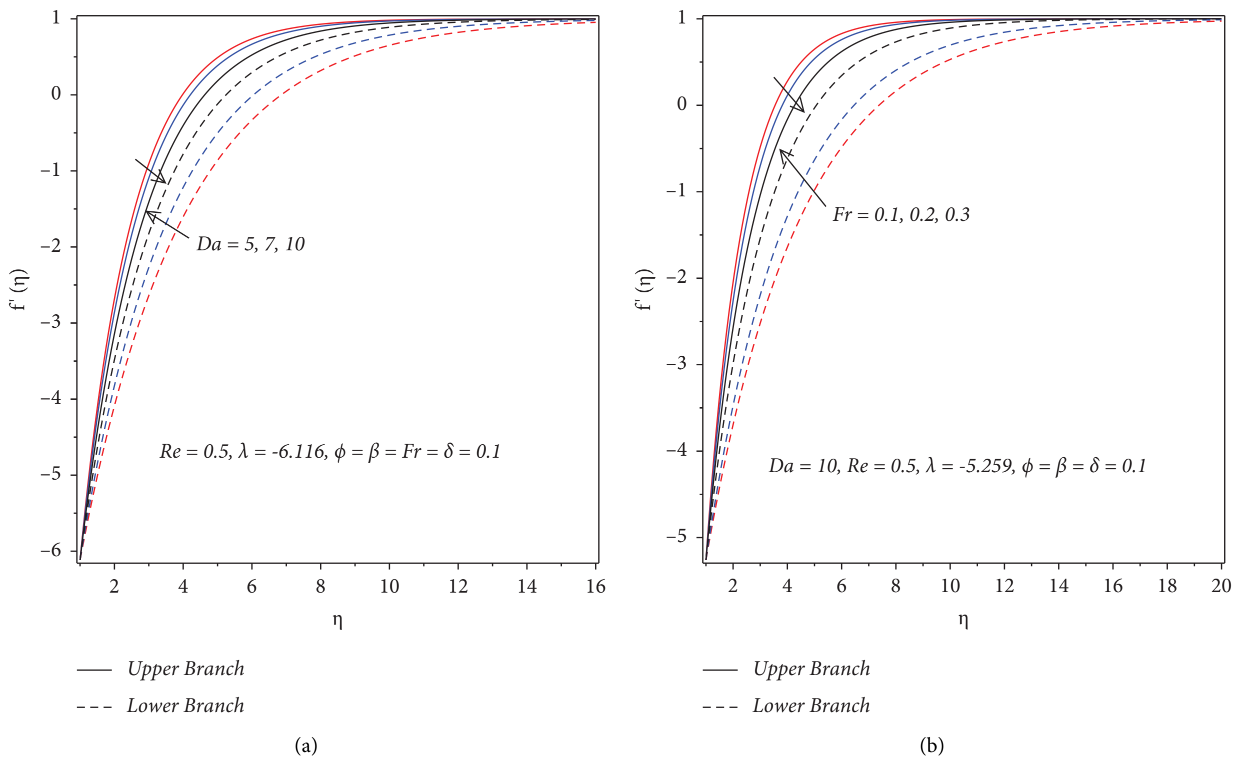

Figure 14: Velocity profile for shrinking parameter with (a) Da and (b) Fr.

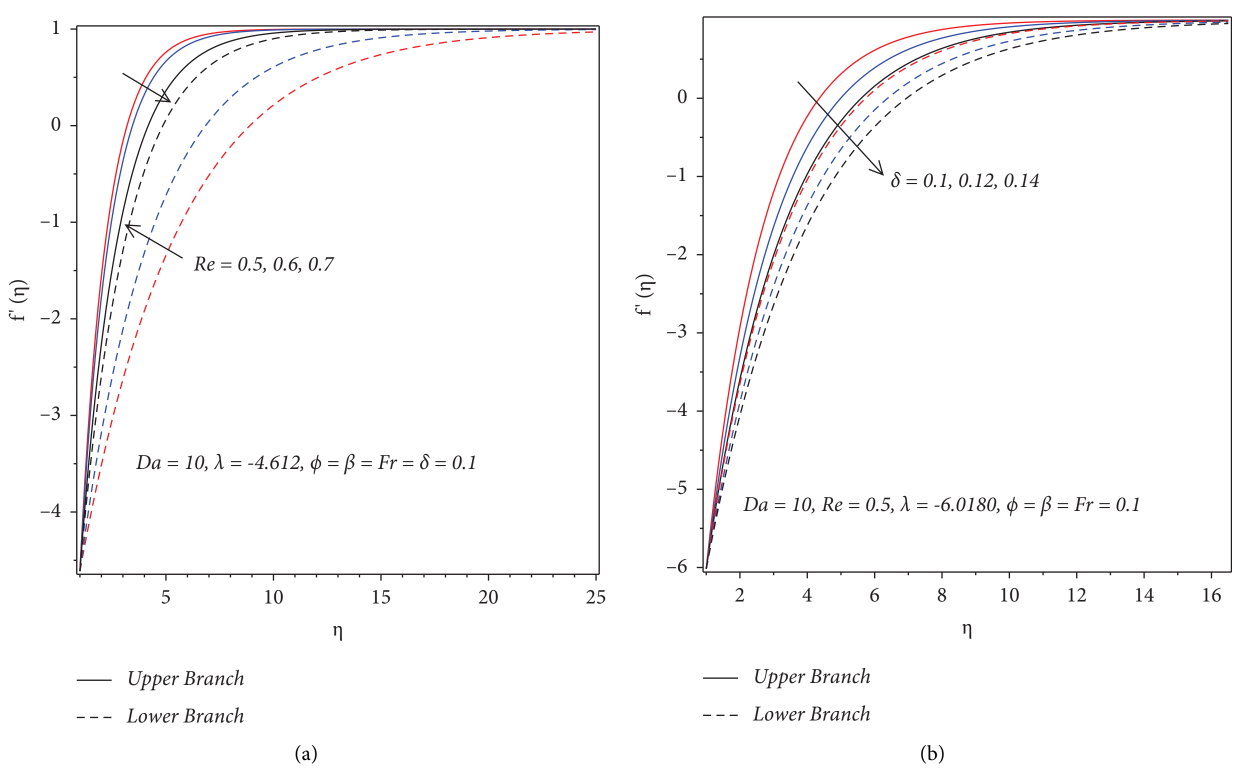

Figure 15: Velocity profile for shrinking parameter with (a) Re and (b) δ.

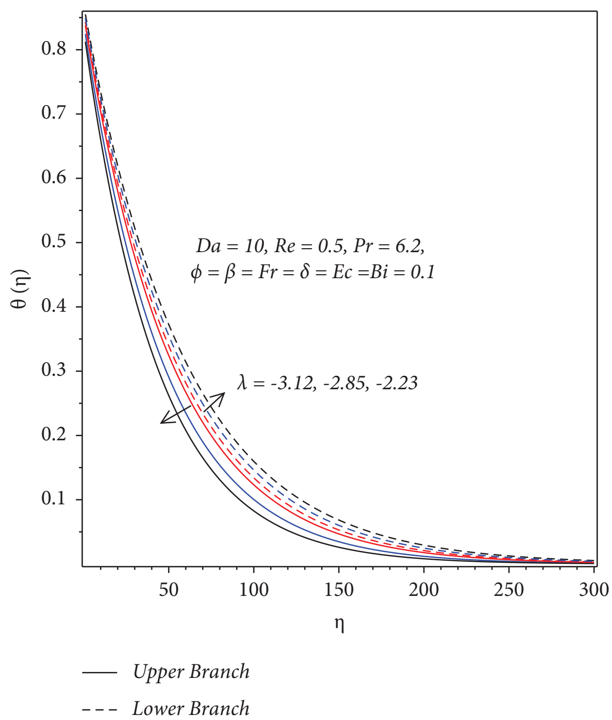

FIGURE 16: Temperature profile for the shrinking parameter with λ.

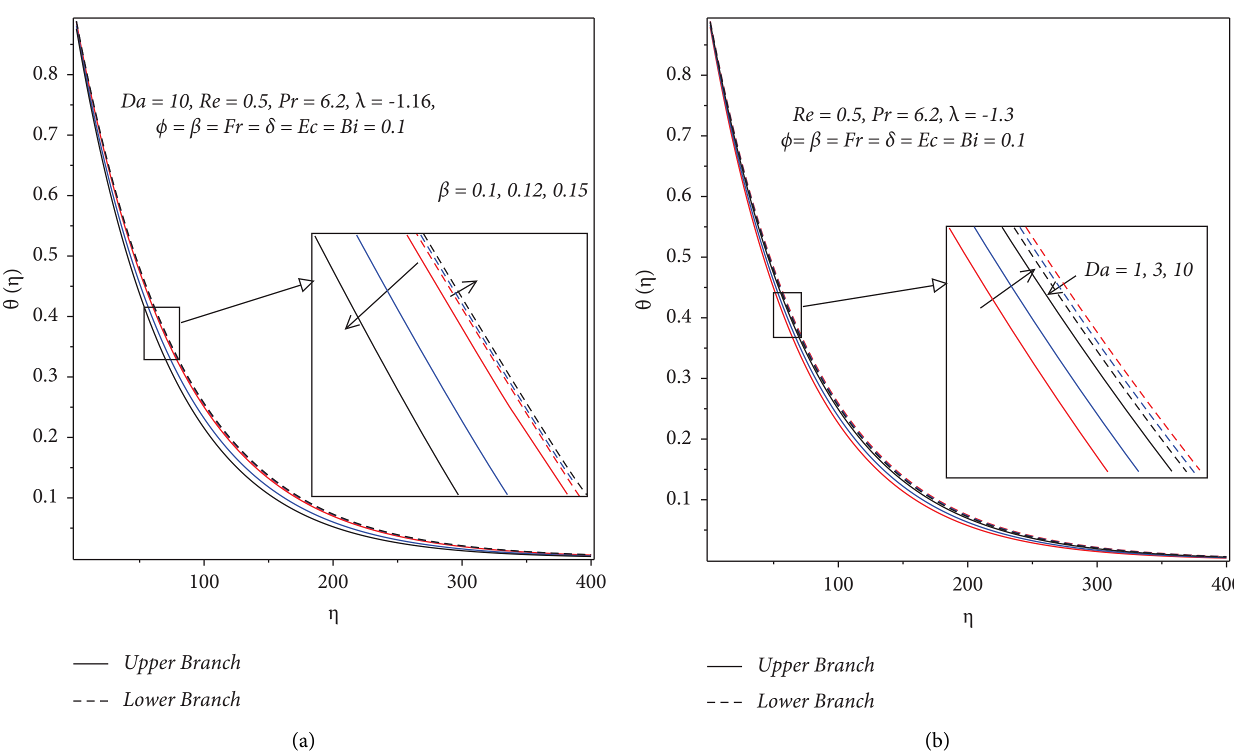

FIGURE 17: Temperature profile for the shrinking parameter with (a) β and (b) Da.

The effect of the Prandtl number Pr on the thermal properties of the Casson nanofluid flows is revealed, and it is observed that as Pr upsurges, the temperature and its boundary layer thickness diminish for the upper branch solutions, as presented in Figure 19(b). Figure 20(a) illustrates the influence of the viscous dissipation parameter (Eckert number Ec) on the thermal profile. The rising of both the temperature profile and the boundary layer thickness are

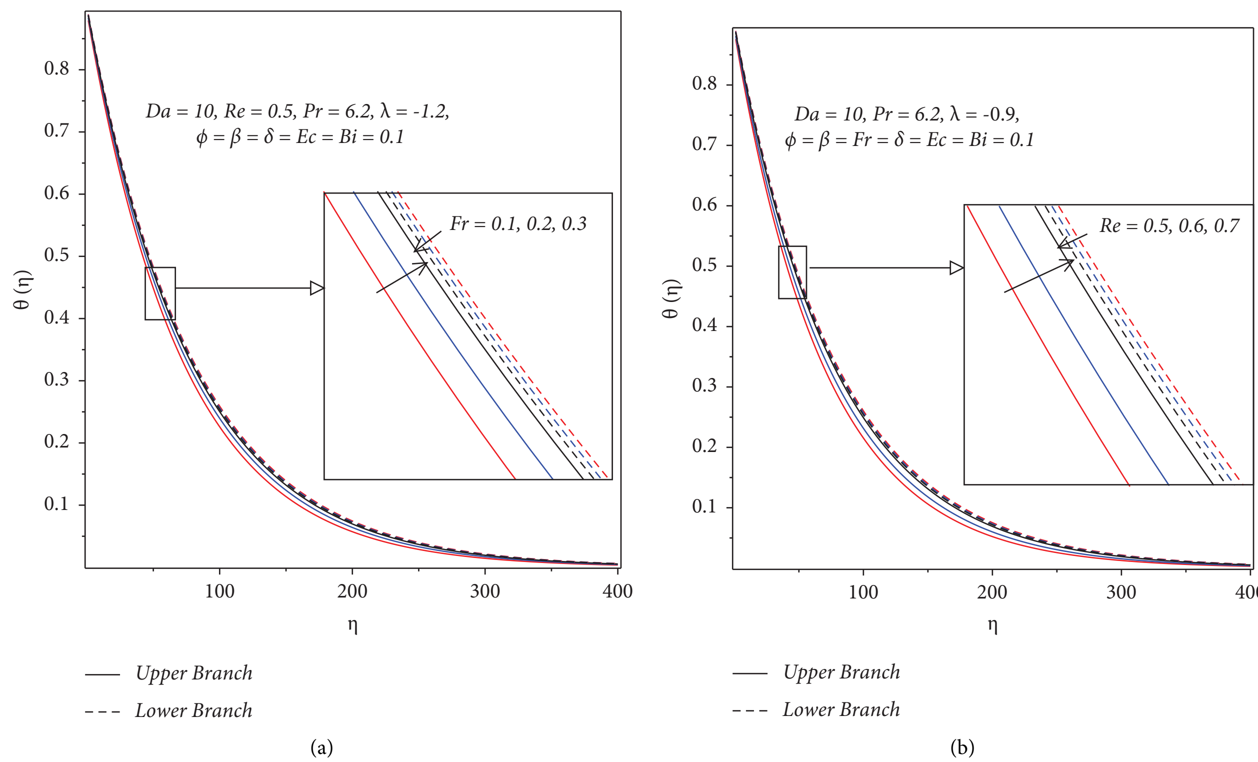

FIGURE 18: Temperature profile for the shrinking parameter with (a) Fr and (b) Re.

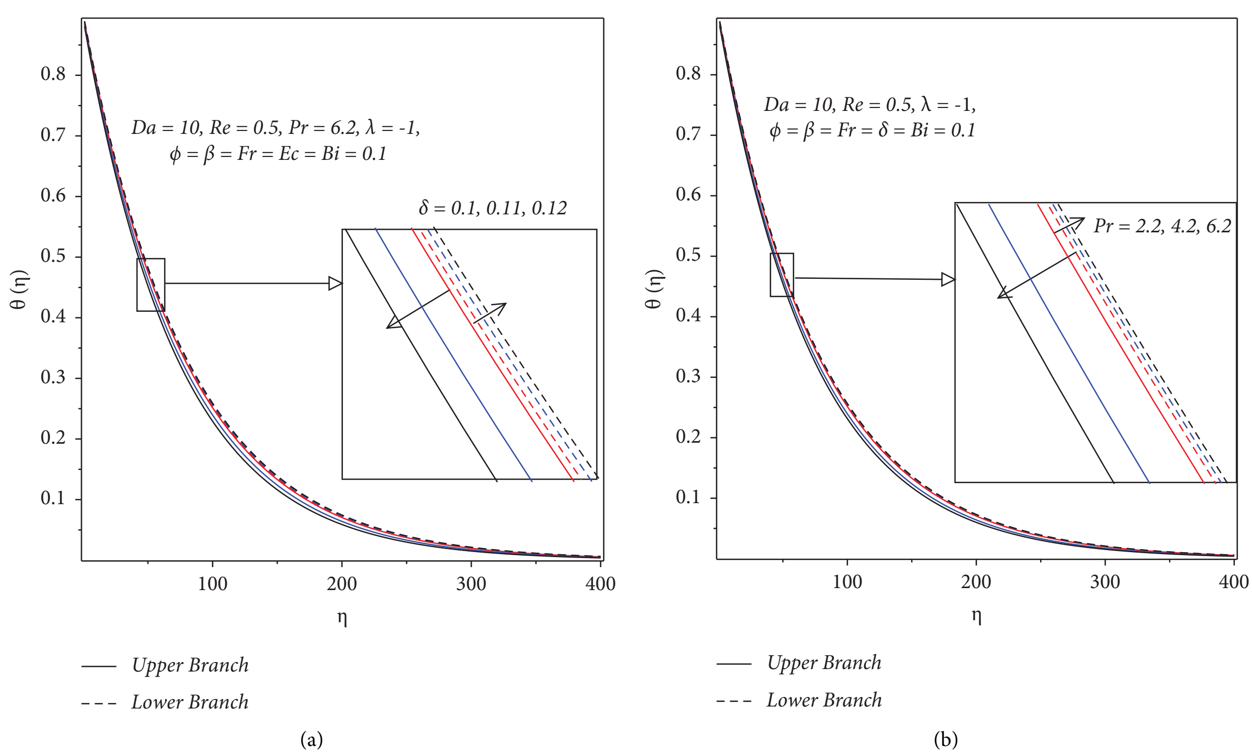

FIGURE 19: Temperature profile for the shrinking parameter with (a) δ and (b) Pr.

observed at the expense of enhancing the viscous dissipation parameter Ec for the upper branch solution. It is known that the kinetic energy is absorbed by viscosity from the fluid motion and converted into internal energy that raises the heating of the fluid flow, thus increasing both the temperature profile and its boundary layer thickness.

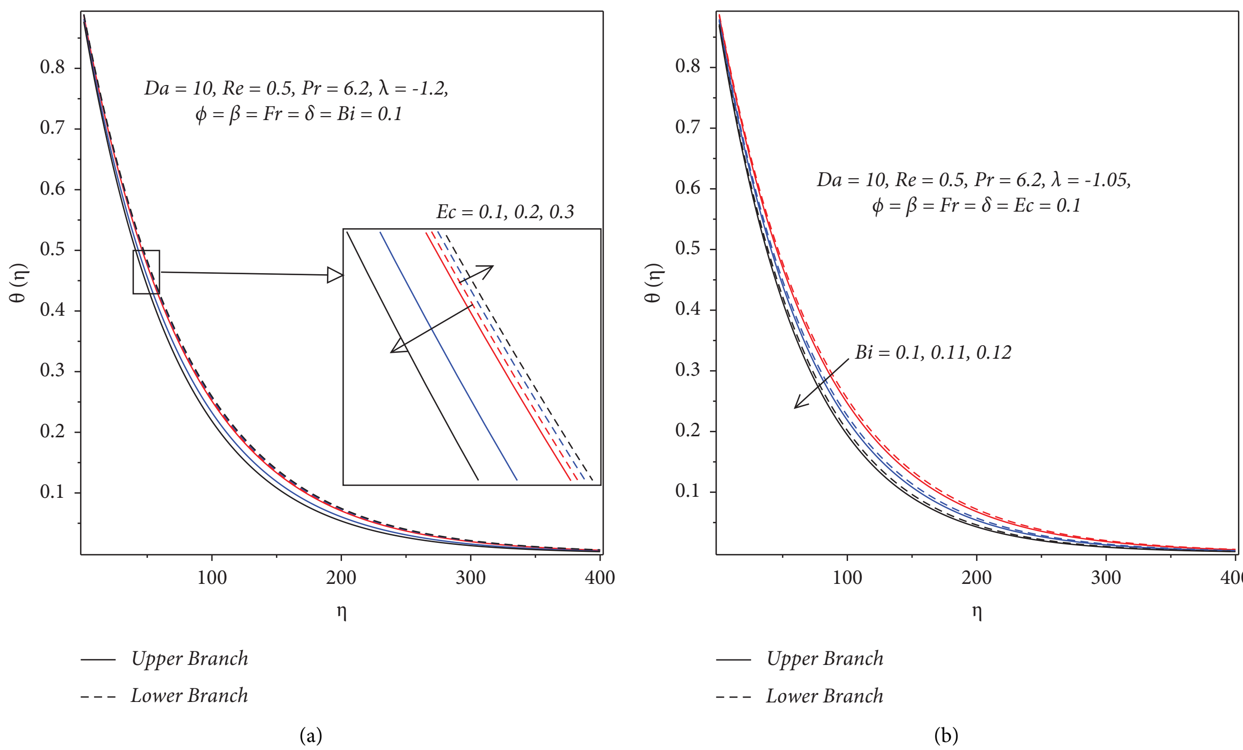

Figure 20: Temperature profile for the shrinking parameter with (a) *Ec* and (b) *Bi*.

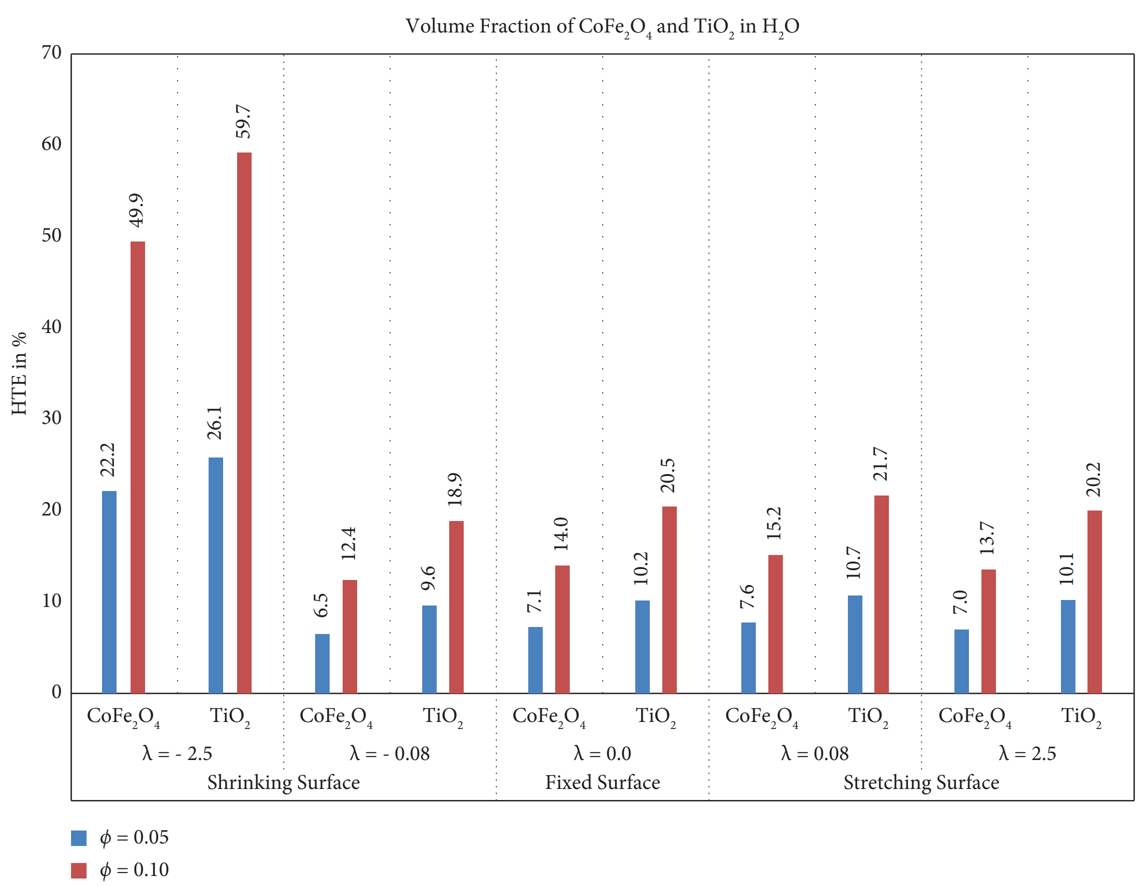

Figure 21: Percentage heat transfer enhancement for varying values of ϕ, whereas $\beta = 5, Pr = 6.2, Da = 10, Re = 0.5, Fr = \delta = Ec = Bi = 0.1$ for both $CoFe_2O_4$ and TiO_2 nanoparticles application.

Figure 20(b) depicts that increasing the convective heating parameter Bi drops the temperature profile and the related boundary layer thickness of Casson nanofluid flow for the upper branch solution. Physically, for $Bi < 1$, the temperature on the surface and beneath the surface (inside the cylinder) will be approximately similar, and/or the surface is a good conductor of heat, so the temperature is uniformly distributed throughout the surface of the cylinder.

As the velocity ratio λ increases, the temperature profile drops and the thermal boundary layer diminishes for the upper branch solutions, as depicted in Figure 16.

Generalizing based on the plots under discussion and Table 6, the temperature profile is higher for CF compared to TD for the upper branch solutions. Moreover, nearer to λ_c, temperature profile and its thermal boundary layer decrease for increasing values of β, Pr, Ec, and Bi; however, the opposite trend holds far from λ_c (say at $\lambda = -0.1$).

6.6. Heat Transfer Enhancement. The chart in Figure 21 demonstrates how the rate of heat transfer is enhanced for increasing values of the nanoparticles' cobalt ferrite ($CoFe_2O_4$) and/or titanium dioxide (TiO_2) volume fraction ϕ in the Casson fluid for the shrinking, fixed, and stretching surfaces. The heat transfer enhancement is more pronounced for TiO_2 nanoparticles compared to that of $CoFe_2O_4$ nanoparticles, which could be due to the larger thermal conductivity of TD with respect to CF. Moreover, the rate of heat transfer enhancement is higher for the working Casson nanofluids with increasing nanoparticle volume fraction ϕ for a higher shrinking parameter compared to other cases. Studies revealed that nanoparticles serve as better coolants for industrial and engineering usage when compared to base fluids; for instance, TD can be used as a better enhancer of heat transfer rate and cooling of radiators and electronic devices, etc.

7. Conclusions

Numerical investigation into the stagnation point flow of $CoFe_2O_4/TiO_2$-H_2O-Casson nanofluid past a slippery surface stretching/shrinking through a Darcy–Forchheimer porous medium in the presence of viscous dissipation and convective heating has been worked out. By using similarity transformations, the modeled boundary layer PDEs were converted into a system of ODEs with their corresponding boundary conditions, and the shooting technique with bvp solver embedded in Maple software packages was used for the numerical computation of the solutions. The temporal stability analysis has been done to identify stable and physically reliable solutions subjected to small disturbances. The effect of various parameters on the dimensionless velocity and temperature profiles, the coefficient of skin friction, and rates of heat transfer and enhancement are obtained numerically and presented in graphs, tables, and a chart. The following findings are summarized from the discussion:

(i) There is a critical value of the shrinking parameter λ_c that determines the interval of solutions, such that the critical value $|\lambda_c|$ widens only for higher values of nanoparticle volume fraction and slipperiness parameters, and increment in $|\lambda_c|$ is higher for TiO_2 than $CoFe_2O_4$.

(ii) The skin friction (drag force) coefficient of flow escalates only as the nanoparticle volume fraction parameter increases and reduces with an increment in the values of other parameters for the upper branch solutions.

(iii) For the shrinking surface nearer to the critical shrinking parameter λ_c, the coefficient of skin friction increasingly overshot as λ rises for all parameters (ϕ, β, Da, Fr, Re, and δ), resulting in a reduced velocity profile with increasing momentum boundary layer thickness for all parameters in the upper branch solutions.

(iv) For the shrinking surface, there are unobservable effects of Pr, Ec, and Bi on flow velocity profile and coefficient of skin friction nearer to the fixed surface.

(v) For the shrinking surface, the increment in Da, Fr, and Re declines the heat transfer rate and raises the thermal behavior the Casson nanofluid near λ_c, and the reverse is observed nearer to the fixed cylindrical surface.

(vi) The coefficient of skin friction (drag force) and the temperature profile are a decreasing function of the shrinking parameter λ; however, the reverse is true for the velocity profile and rate of heat transfer in the upper branch solutions.

(vii) For the upper branch solutions, the rate of heat transfer drops for increasing values of the nanoparticle volume fraction parameter, Forchheimer parameter, and Biot number nearer to λ_c and upsurges for the other parameters.

(viii) Increasing the amount of nanoparticle volume fraction in the Casson fluid boosts the heat transfer enhancement rate, which is higher for TiO_2 than $CoFe_2O_4$.

(ix) The temporal stability analysis determined the smallest eigenvalue ε which revealed that only the upper branch solution is stable and physically realizable, whereas the lower branch solution is unstable and not realistic for the flow problem.

(x) For the upper branch solutions, the velocity profile drops with all parameters nearer to λ_c and enhances with an increment in the values of the nanoparticle volume fraction parameter, slipperiness parameter, Darcy number, and Reynolds number far from λ_c for the shrinking surface.

(xi) For the upper branch solutions, the temperature profile and thermal boundary layer thickness increase only with enhancing values of nanoparticle volume fractions and porous inertia resistance parameters nearer to λ_c, and increase the nanoparticle volume fraction parameter, Casson factor, Prandtl number, Eckert number, and Biot number far from λ_c.

(xii) For the Newtonian flow (as $\beta \longrightarrow \infty$), the critical shrinking parameter $|\lambda_c|$, surface drag force coefficient, velocity profile, and temperature profile with its boundary layer thickness diminish, whereas the heat transfer rate and momentum boundary layer rise for the upper branch solutions nearer to λ_c.

(xiii) The critical shrinking parameter $|\lambda_c|$ and heat transfer rate and enhancement are higher for TiO_2 nanoparticles compared to $CoFe_2O_4$ nanoparticles, whereas the skin friction coefficient, velocity, and temperature profiles are higher for $CoFe_2O_4$ nanoparticles relative to TiO_2 for the upper branch solutions.

Nomenclature

a: Radius of the cylinder (m)
b, c: Real constants (s^{-1})
Bi: Biot number $(= a^2 h_f/2rk_f)$
C_f: Coefficient of the skin friction
C_p: Specific heat at constant pressure of the fluid $(\mathrm{Jkg^{-1}K^{-1}})$
Da: Darcy number (porous media parameter) $(= 2ck_1/\nu_f)$
e_{ij}: The rate of strain tensor
Ec: Eckert number $(= U_\infty^2/(C_p)_f(T_f - T_\infty))$
f: Dimensionless stream function
F: Forchheimer drag force coefficient m^{-1}
F_r: Forchheimer parameter $(= zF/\rho_f\sqrt{k_1})$
h_f: Convective heat transfer coefficient $(\mathrm{Wm^{-2}K^{-1}})$
k_1: Porous medium permeability (m^2)
k_f: Thermal conductivity of the base fluid $(\mathrm{Wm^{-1}K^{-1}})$
k_s: Nanoparticles' thermal conductivity $[\mathrm{Wm^{-1}K^{-1}}]$
k_{nf}: Nanofluids' effective thermal conductivity $[\mathrm{Wm^{-1}K^{-1}}]$
L: Slip length coefficient $(\mathrm{Kgm^{-1}s^{-2}})$
n: Real constant $(\mathrm{Km^{-2}})$
Nu_z: Local Nusselt number
Pr: Prandtl number $(= \nu_f(\rho C_p)_f/k_f)$
p_y: Yield stress of the fluid (Nm^{-2})
q_w: Heat flux (Wm^{-2})
Re: Reynolds number $(= a^2c/2\nu_f)$
T: Temperature of the fluid (K)
T_f: Local fluid temperature (K)
T_∞: Ambient temperature of the Casson nanofluid (K)
u, v: Velocity components along z, r coordinates, respectively (ms^{-1})
U_∞: Free stream velocity of the Casson fluid (ms^{-1})
z, r: Coordinates along the surface and the radial coordinate, respectively (m)

Greek Symbols

β: Non-Newtonian/Casson parameter/factor
δ: Velocity slip parameter $(= 2r\mu_f/a^2L)$
ε: Eigenvalue parameter
η: Similarity variable
θ: Dimensionless temperature
λ: Velocity ratio (stretching/shrinking) parameter $(= b/c)$
μ_B: The plastic dynamic viscosity of the Casson nanofluid $(\mathrm{Nm^{-2}s})$
μ_f: Dynamic viscocity of the base fluid $(\mathrm{kgm^{-1}}s^{-2})$
μ_{nf}: Effective dynamic viscosity of the Casson nanofluid $(\mathrm{kgms^{-2}})$
ν_f: Base fluids' kinematic viscosity (m^2s^{-1})
π: The $(i, j)^{\text{th}}$ component of deformation rate $(\mathrm{Nm^{-2}})$
π_c: Critical value of π $(\mathrm{Nm^{-2}})$
ρ_f: Density of the base fluid $(\mathrm{kgm^{-3}})$
ρ_s: Density of the solid nanoparticle $(\mathrm{kgm^{-3}})$
ρ_{nf}: Effective density of the Casson nanofluid $(\mathrm{kgm^{-3}})$
$(\rho C_p)_{nf}$: Effective heat capacity of the Casson nanofluid $(\mathrm{Jm^{-3}K^{-1}})$
τ: Nondimensional time variable
τ_{ij}: Components of stress tensor $(\mathrm{Nm^{-2}})$
τ_w: Wall skin friction $(\mathrm{Nm^{-2}})$
ϕ: Nanoparticles volume fraction.

Data Availability

The data used for supporting the findings of this research are included within the article.

Additional Points

Future Perspective. This present study on nanofluid heat transfer enhancement is valid for Casson nanofluid and did not incorporate the effects of other important factors such as nanoparticle shape factors, hybrid nanoparticles, thermophoresis, and Brownian motion. The authors envisage extending this study in the future to include other non-Newtonian nanofluids (both single-phase and two-phase flow models) as well as the effects of all the omitted factors.

Conflicts of Interest

The authors declare that there are no conflicts of interest.

Acknowledgments

The authors gratefully acknowledge Adama Science and Technology University for facilitating this study.

References

[1] M. Nakamura and T. Sawada, "Numerical study on the flow of a non-newtonian fluid through an axisymmetric stenosis," *J Biomech Eng.*, vol. 110, no. 2, pp. 137–43, 1988.

[2] I. L. Animasaun, "Effects of thermophoresis, variable viscosity and thermal conductivity on free convective heat and mass transfer of non-darcian mhd dissipative casson fluid flow with suction and nth order of chemical reaction," *Journal of the Nigerian Mathematical Society*, vol. 34, no. 1, pp. 11–31, 2015.

[3] G. Rasool, A. J. Chamkha, T. Muhammad, A. Shafiq, and I. Khan, "Darcy-forchheimer relation in casson type mhd nanofluid flow over non-linear stretching surface," *Propulsion and Power Research*, vol. 9, no. 2, pp. 159–168, 2020.

[4] H. Khan, F. Ali, N. Khan, I. Khan, and A. Mohamed, "Electromagnetic flow of casson nanofluid over a vertical riga

plate with ramped wall conditions," *Frontiers in Physics*, vol. 903, 2022.

[5] H. Alkasasbeh, "Numerical solution of heat transfer flow of casson hybrid nanofluid over vertical stretching sheet with magnetic field effect," *CFD Letters*, vol. 14, no. 3, pp. 39–52, 2022.

[6] F. B. Tadesse, O. D. Makinde, and L. G. Enyadene, "Hydromagnetic stagnation point flow of a magnetite ferrofluid past a convectively heated permeable stretching/shrinking sheet in a Darcy–forchheimer porous medium," *Sādhanā*, vol. 46, no. 3, pp. 115–117, 2021.

[7] M. Kazemi, M. Ghobadi, and A. Mirzaie, "Cobalt ferrite nanoparticles ($CoFe_2O_4$ MNPs) as catalyst and support: magnetically recoverable nanocatalysts in organic synthesis (CoFe2O4 MNPs) as catalyst and support: magnetically recoverable nanocatalysts in organic synthesis," *Nanotechnology Reviews*, vol. 7, no. 1, pp. 43–68, 2018.

[8] H. M. Ali, M. Usman Sajid, and A. Arshad, "Heat transfer applications of TiO2nanofluids," *Application of titanium dioxide*, vol. 26, 2017.

[9] F. Mebarek and I. Chabani, "Review on nano-fluids applications and heat transfer enhancement techniques in different enclosures," *Journal of Nanofluids*, vol. 11, no. 2, pp. 155–168, 2022.

[10] N. V. Ganesh, A. Abdul Hakeem, and B. Ganga, "Darcy–forchheimer flow of hydromagnetic nanofluid over a stretching/shrinking sheet in a thermally stratified porous medium with second order slip, viscous and ohmic dissipations effects," *Ain Shams Engineering Journal*, vol. 9, no. 4, pp. 939–951, 2018.

[11] M. Jawad, Z. Shah, S. Islam, E. Bonyah, and A. Z. Khan, "Darcy-forchheimer flow of mhd nanofluid thin film flow with joule dissipation and Navier's partial slip," *Journal of Physics Communications*, vol. 2, no. 11, Article ID 115014, 2018.

[12] A. Bisht and R. Sharma, "Computation of Darcy-forchheimer flow of sisko nanofluid over a stretching cylinder," *Heat Transfer*, vol. 50, no. 8, pp. 7712–7732, 2021.

[13] K. Singh, A. K. Pandey, and M. Kumar, "Melting heat transfer assessment on magnetic nanofluid flow past a porous stretching cylinder," *Journal of the Egyptian Mathematical Society*, vol. 29, no. 1, pp. 1–14, 2021.

[14] T. Poornima, P. Sreenivasulu, and B. Souayeh, "Mathematical study of heat transfer in a stagnation flow of a hybrid nanofluid over a stretching/shrinking cylinder," *Journal of Engineering Physics and Thermophysics*, vol. 95, no. 6, pp. 1443–1454, 2022.

[15] N. Najib, N. Bachok, N. F. Dzulkifli, and I. Pop, "Numerical results on slip effect over an exponentially stretching/shrinking cylinder," *Mathematics*, vol. 10, no. 7, p. 1114, 2022.

[16] K. A. Duguma, O. Daniel Makinde, and L. G. Enyadene, "Dual solutions and stability analysis of Cu-H2O-casson nanofluid convection past a heated stretching/shrinking slippery sheet in a porous medium," *Computational and Mathematical Methods*, vol. 2023, Article ID 6671523, 20 pages, 2023.

[17] K. A. Duguma, O. D. Makinde, and L. G. Enyadene, "Stability analysis of dual solutions of convective flow of casson nanofluid past a shrinking/stretching slippery sheet with thermophoresis and brownian motion in porous media," *Journal of Mathematics*, vol. 2023, Article ID 5954860, 25 pages, 2023.

[18] P. D. Weidman, A. M. J. Davis, and D. G. Kubitschek, "Crocco variable formulation for uniform shear flow over a stretching surface with transpiration: multiple solutions and stability," *Zeitschrift für Angewandte Mathematik und Physik*, vol. 59, no. 2, pp. 313–332, 2008.

[19] S. Das, A. Ali, and R. N. Jana, "Darcy–forchheimer flow of a magneto-radiated couple stress fluid over an inclined exponentially stretching surface with ohmic dissipation," *World Journal of Engineering*, vol. 18, no. 2, pp. 345–360, 2020.

[20] C. Y. Wang, "Stagnation flow towards a shrinking sheet," *International Journal of Non-linear Mechanics*, vol. 43, no. 5, pp. 377–382, 2008.

[21] L. A. Lund, A. F. Chandio, N. Vrinceanu, U. Yashkun, Z. Shah, and A. Alshehri, "Darcy–forchheimer magnetized nanofluid flow along with heating and dissipation effects over a shrinking exponential sheet with stability analysis," *Micromachines*, vol. 14, no. 1, p. 106, 2022.

[22] M. Ferdows, J. Alam, G. Murtaza, E. E. Tzirtzilakis, and S. Sun, "Biomagnetic flow with CoFe2O4 magnetic particles through an unsteady stretching/shrinking cylinder," *Magnetochemistry*, vol. 8, no. 3, p. 27, 2022.

[23] R. S. R. Gorla, "Heat transfer in an axisymmetric stagnation flow on a cylinder," *Applied Scientific Research*, vol. 32, no. 5, pp. 541–553, 1976.

[24] R. S. R. Gorla, "Mixed convection in an axisymmetric stagnation flow on a vertical cylinder," *Acta Mechanica*, vol. 99, no. 1-4, pp. 113–123, 1993.

[25] S. D. Harris, D. B. Ingham, and I. Pop, "Mixed convection boundary-layer flow near the stagnation point on a vertical surface in a porous medium: brinkman model with slip," *Transport in Porous Media*, vol. 77, no. 2, pp. 267–285, 2009.

[26] T. A. M. Shatnawi, N. Abbas, and W. Shatanawi, "Mathematical analysis of unsteady stagnation point flow of radiative casson hybrid nanofluid flow over a vertical riga sheet," *Mathematics*, vol. 10, no. 19, p. 3573, 2022.

[27] H. T. Basha and R. Sivaraj, "Stability analysis of casson nanofluid flow over an extending/contracting wedge and stagnation point," *Journal of Applied and Computational Mechanics*, vol. 8, no. 2, pp. 566–579, 2022.

[28] M. A. S. Murad, F. K. Hamasalh, and H. F. Ismael, "Numerical study of stagnation point flow of casson-carreau fluid over a continuous moving sheet," *AIMS Mathematics*, vol. 8, no. 3, pp. 7005–7020, 2023.

[29] N. Bachok, A. Ishak, and I. Pop, "Stagnation-point flow over a stretching/shrinking sheet in a nanofluid," *Nanoscale Research Letters*, vol. 6, no. 1, pp. 623–710, 2011.

[30] N. Najib, N. Bachok, N. M. Arifin, and A. Ishak, "Stagnation point flow and mass transfer with chemical reaction past a stretching/shrinking cylinder," *Scientific Reports*, vol. 4, no. 1, pp. 4178–4187, 2014.

[31] N. S. Omar, N. Bachok, and N. M. Arifin, "Stagnation point flow over a stretching or shrinking cylinder in a copper-water nanofluid," *Indian Journal of Science and Technology*, vol. 8, no. 31, pp. 1–7, 2015.

[32] T. Hayat, M. I. Khan, M. Waqas, A. Alsaedi, and M. Farooq, "Numerical simulation for melting heat transfer and radiation effects in stagnation point flow of carbon-water nanofluid," *Computer Methods in Applied Mechanics and Engineering*, vol. 315, no. C, pp. 1011–1024, 2017.

[33] M. M. Nandeppanavar and S. Shakunthala, "Heat transfer analysis of stagnation point flow over a stretching cylinder in a suspension of carbon nanotube," *Journal of Nanofluids*, vol. 6, no. 6, pp. 1173–1180, 2017.

[34] S. Nadeem, N. Abbas, and A. U. Khan, "Characteristics of three dimensional stagnation point flow of hybrid nanofluid past a circular cylinder," *Results in Physics*, vol. 8, pp. 829–835, 2018.

[35] K. A. Kumar, V. Sugunamma, N. Sandeep, and J. V. R. Reddy, "MHD stagnation point flow of Williamson and Casson fluids past an extended cylinder: a new heat flux model," *SN Applied Sciences*, vol. 1, no. 7, p. 705, 2019.

[36] A. B. Rahimi, H. Mohammadiun, and M. Mohammadiun, "Self-similar solution of radial stagnation point flow and heat transfer of a viscous, compressible fluid impinging on a rotating cylinder," *Iranian Journal of Science and Technology, Transactions of Mechanical Engineering*, vol. 43, no. S1, pp. 141–153, 2019.

[37] L. A. Lund, Z. Omar, I. Khan, D. Baleanu, and K. S. Nisar, "Dual similarity solutions of mhd stagnation point flow of casson fluid with effect of thermal radiation and viscous dissipation: stability analysis," *Scientific Reports*, vol. 10, no. 1, pp. 15405–15413, 2020.

[38] R. Alizadeh, N. Karimi, and A. Nourbakhsh, "Effects of radiation and magnetic field on mixed convection stagnation-point flow over a cylinder in a porous medium under local thermal non-equilibrium," *Journal of Thermal Analysis and Calorimetry*, vol. 140, no. 3, pp. 1371–1391, 2020.

[39] N. S. Khashi'ie, E. H. Hafidzuddin, N. M. Arifin, and N. Wahi, "Stagnation point flow of hybrid nanofluid over a permeable vertical stretching/shrinking cylinder with thermal stratification effect," *CFD Letters*, vol. 12, no. 2, pp. 80–94, 2020.

[40] M. Hussain and M. Sheremet, "Convection analysis of the radiative nanofluid flow through porous media over a stretching surface with inclined magnetic field," *International Communications in Heat and Mass Transfer*, vol. 140, Article ID 106559, 2023.

[41] T. Hayat, T. Muhammad, S. Al-Mezal, and S. J. Liao, "Darcy-forchheimer flow with variable thermal conductivity and cattaneo-christov heat flux," *International Journal of Numerical Methods for Heat and Fluid Flow*, vol. 26, no. 8, pp. 2355–2369, 2016.

[42] J. Zhang, F. Wang, M. Tamoor et al., "Influence of chemical reaction on mhd Newtonian fluid flow on vertical plate in porous medium in conjunction with thermal radiation," *Open Physics*, vol. 20, no. 1, pp. 302–312, 2022.

[43] J. H. Merkin, "On dual solutions occurring in mixed convection in a porous medium," *Journal of Engineering Mathematics*, vol. 20, no. 2, pp. 171–179, 1986.

[44] O. D. Makinde, "Stagnation point flow with heat transfer and temporal stability of ferrofluid past a permeable stretching/shrinking sheet," *Defect and Diffusion Forum*, vol. 387, pp. 510–522, 2018.

[45] R. Alizadeh, N. Karimi, A. Mehdizadeh, and A. Nourbakhsh, "Analysis of transport from cylindrical surfaces subject to catalytic reactions and non-uniform impinging flows in porous media," *Journal of Thermal Analysis and Calorimetry*, vol. 138, no. 1, pp. 659–678, 2019.

[46] K. Hong, R. Alizadeh, M. V. Ardalan et al., "Numerical study of nonlinear mixed convection inside stagnation-point flow over surface-reactive cylinder embedded in porous media," *Journal of Thermal Analysis and Calorimetry*, vol. 141, no. 5, pp. 1889–1903, 2020.

[47] R. L. Hamilton and O. K. Crosser, "Thermal conductivity of heterogeneous two-component systems," *Industrial and Engineering Chemistry Fundamentals*, vol. 1, no. 3, pp. 187–191, 1962.

[48] K. S. Tshivhi and O. D. Makinde, "Magneto-nanofluid coolants past heated shrinking/stretching surfaces: dual solutions and stability analysis," *Results in Engineering*, vol. 10, Article ID 100229, 2021.

[49] S. Shaw, A. S. Dogonchi, M. K. Nayak, and O. D. Makinde, "Impact of entropy generation and nonlinear thermal radiation on Darcy-Forchheimer flow of MnFe 2 O 4-Casson/water nanofluid due to a rotating disk: application to brain dynamics," *Arabian Journal for Science and Engineering*, vol. 45, no. 7, pp. 5471–5490, 2020.

[50] S. W. Joseph, R. R. Colwell, and J. B. Kaper, "Vibrio parahaemolyticus and related halophilic vibrios," *CRC Critical Reviews in Microbiology*, vol. 10, no. 1, pp. 77–124, 1982.

[51] P. D. Weidman, D. G. Kubitschek, and A. M. J. Davis, "The effect of transpiration on self-similar boundary layer flow over moving surfaces," *International Journal of Engineering Science*, vol. 44, no. 11-12, pp. 730–737, 2006.

[52] C. Y. Wang, "Axisymmetric stagnation flow on a cylinder," *Quarterly of Applied Mathematics*, vol. 32, no. 2, pp. 207–213, 1974.